First order controls of avulsion in river deltas

Octria Adi Prasojo[1], Trevor B. Hoey[2], Amanda Owen[1], and Richard David Williams[1]

[1]University of Glasgow
[2]Brunel University London

September 13, 2023

Abstract

Changed hydrological regimes, sea-level rise, and accelerated subsidence are all putting river deltas at risk across the globe. Deltas may respond to these stressors through the mechanism of avulsion. Decades of delta avulsion studies have resulted in conflicting hypotheses that avulsion frequency and location are upstream (water and sediment discharge) or downstream (backwater and sea-level rise) controlled. In this study, we use Delft3D morphodynamic simulations to investigate the main controls over delta avulsion. Avulsion timing and location were recorded in six scenarios modelled over a 400-year period with varying alluvial slopes upstream of a delta slope break (1.13x10-4 to 3.04x10-3) within a range representative global deltas. We measure several independent morphometric variables including avulsion length, delta lobe width, channel width at avulsion, delta topset slope and sediment load. Correlating these variables with the avulsion timescales observed in our model shows that avulsion timescale is mostly controlled by sediment load, which in turn is controlled by the alluvial slope upstream of a delta slope break. With higher stream power index in steeper alluvial slopes, more sediment can be carried within a channel, resulting in more frequent avulsions. Our results are consistent with the avulsion timescale derived from an analytical solution, 19 natural deltas and downscaled physical laboratory deltas. These results help mitigate delta avulsion risk by focusing management efforts on variables that primarily control avulsion in a river delta, but also induce further debate over whether sea-level rise may, or may not, trigger more avulsions in river deltas.

Hosted file

`973141_0_supp_11349366_s0gpkk.docx` available at https://authorea.com/users/663697/articles/665778-first-order-controls-of-avulsion-in-river-deltas

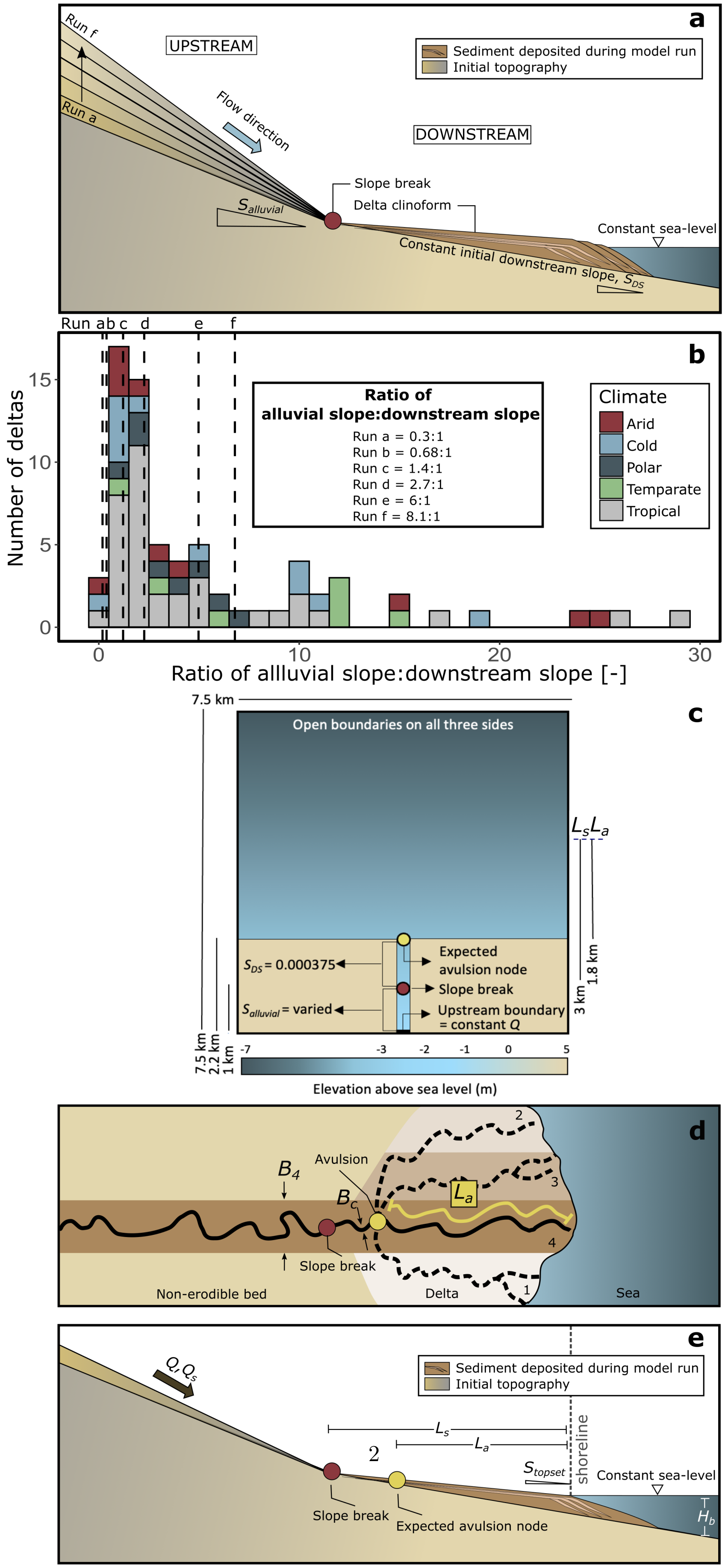

a
Run f
Run a
UPSTREAM
DOWNSTREAM
Flow direction
Sediment deposited during model run
Initial topography
Slope break
Delta clinoform
$S_{alluvial}$
Constant sea-level
Constant initial downstream slope, S_{DS}
b
Run a b c d e f
Number of deltas
Ratio of alluvial slope:downstream slope
Run a = 0.3:1
Run b = 0.68:1
Run c = 1.4:1
Run d = 2.7:1
Run e = 6:1
Run f = 8.1:1
Climate
Arid
Cold
Polar
Temparate
Tropical
Ratio of allluvial slope:downstream slope [-]
c
7.5 km
Open boundaries on all three sides
$L_s L_a$
1.8 km
3 km
S_{DS} = 0.000375
Expected avulsion node
Slope break
$S_{alluvial}$ = varied
Upstream boundary = constant Q
7.5 km
2.2 km
1 km
Elevation above sea level (m)
d
B_4
B_c
Avulsion
L_a
Slope break
Non-erodible bed
Delta
Sea
e
Q, Q_s
Sediment deposited during model run
Initial topography
L_s
L_a
2
S_{topset}
shoreline
Constant sea-level
H_b
Slope break
Expected avulsion node

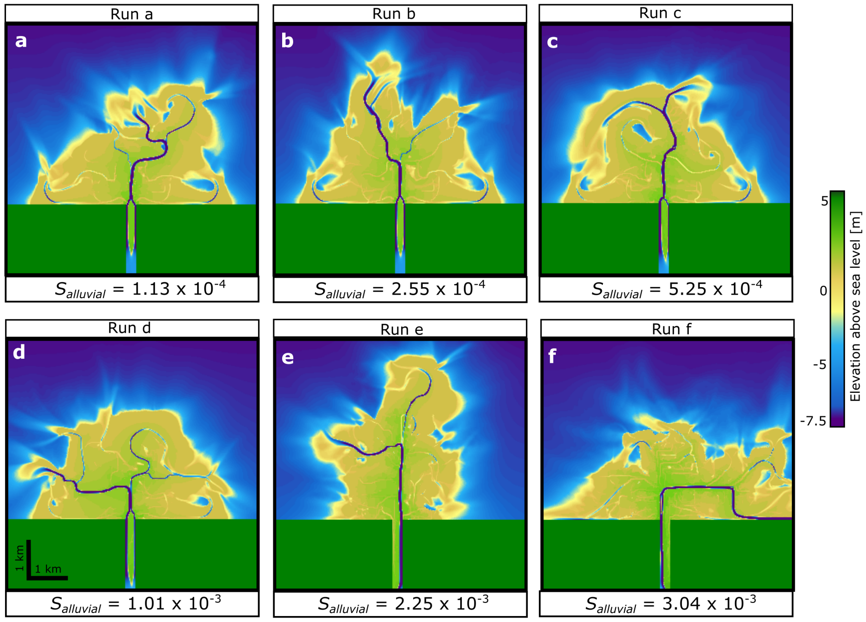

Run a
Run b
Run c
Run d
Run e
Run f
$S_{alluvial}$ = 1.13 x 10^{-4}
$S_{alluvial}$ = 2.55 x 10^{-4}
$S_{alluvial}$ = 5.25 x 10^{-4}
$S_{alluvial}$ = 1.01 x 10^{-3}
$S_{alluvial}$ = 2.25 x 10^{-3}
$S_{alluvial}$ = 3.04 x 10^{-3}
1 km
1 km
Elevation above sea level [m]
5
0
-5
-7.5

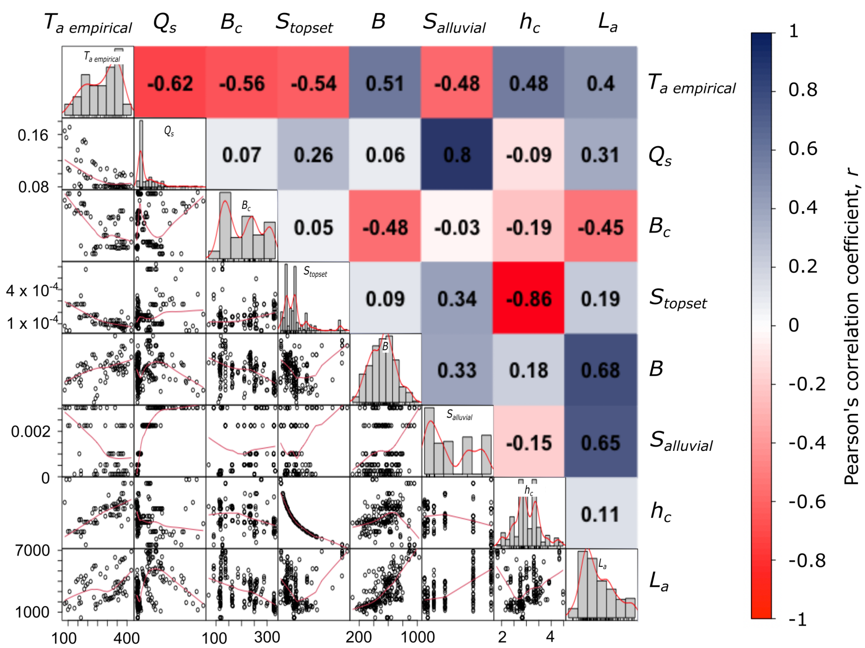

$T_{a\ empirical}$
Q_s
B_c
S_{topset}
B
$S_{alluvial}$
h_c
L_a
-0.62 -0.56 -0.54 0.51 -0.48 0.48 0.4
0.07 0.26 0.06 0.8 -0.09 0.31
0.05 -0.48 -0.03 -0.19 -0.45
0.09 0.34 -0.86 0.19
0.33 0.18 0.68
-0.15 0.65
0.11
Pearson's correlation coefficient, r
1
0.8
0.6
0.4
0.2
0
-0.2
-0.4
-0.6
-0.8
-1

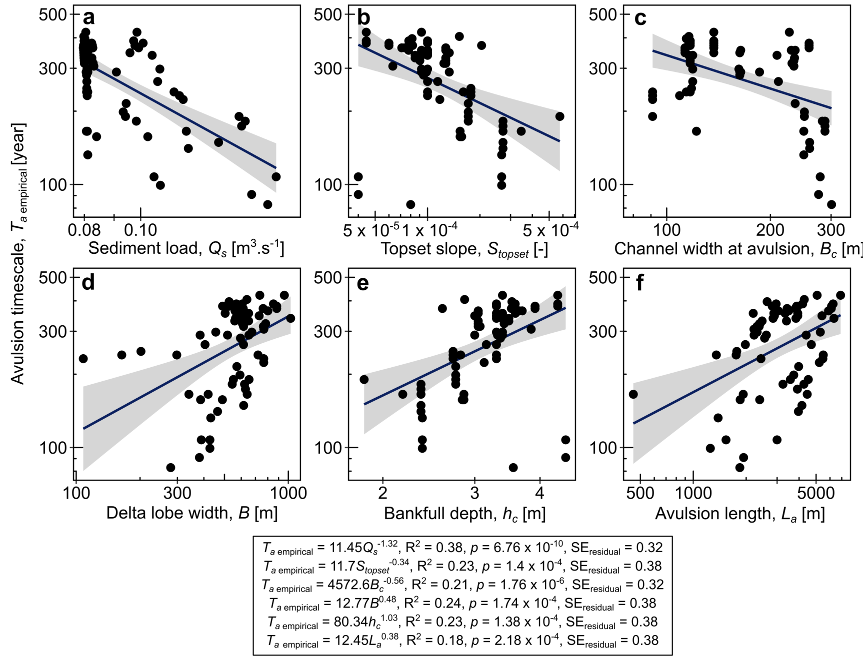
a
b
c
d
e
f
Avulsion timescale, $T_{a\ \mathrm{empirical}}$ [year]
Sediment load, Q_s [m^3.s^{-1}]
Topset slope, S_{topset} [-]
Channel width at avulsion, B_c [m]
Delta lobe width, B [m]
Bankfull depth, h_c [m]
Avulsion length, L_a [m]
$T_{a\ \mathrm{empirical}} = 11.45Q_s^{-1.32}$, $R^2 = 0.38$, $p = 6.76 \times 10^{-10}$, $SE_{\mathrm{residual}} = 0.32$
$T_{a\ \mathrm{empirical}} = 11.7S_{topset}^{-0.34}$, $R^2 = 0.23$, $p = 1.4 \times 10^{-4}$, $SE_{\mathrm{residual}} = 0.38$
$T_{a\ \mathrm{empirical}} = 4572.6B_c^{-0.56}$, $R^2 = 0.21$, $p = 1.76 \times 10^{-6}$, $SE_{\mathrm{residual}} = 0.32$
$T_{a\ \mathrm{empirical}} = 12.77B^{0.48}$, $R^2 = 0.24$, $p = 1.74 \times 10^{-4}$, $SE_{\mathrm{residual}} = 0.38$
$T_{a\ \mathrm{empirical}} = 80.34h_c^{1.03}$, $R^2 = 0.23$, $p = 1.38 \times 10^{-4}$, $SE_{\mathrm{residual}} = 0.38$
$T_{a\ \mathrm{empirical}} = 12.45L_a^{0.38}$, $R^2 = 0.18$, $p = 2.18 \times 10^{-4}$, $SE_{\mathrm{residual}} = 0.38$

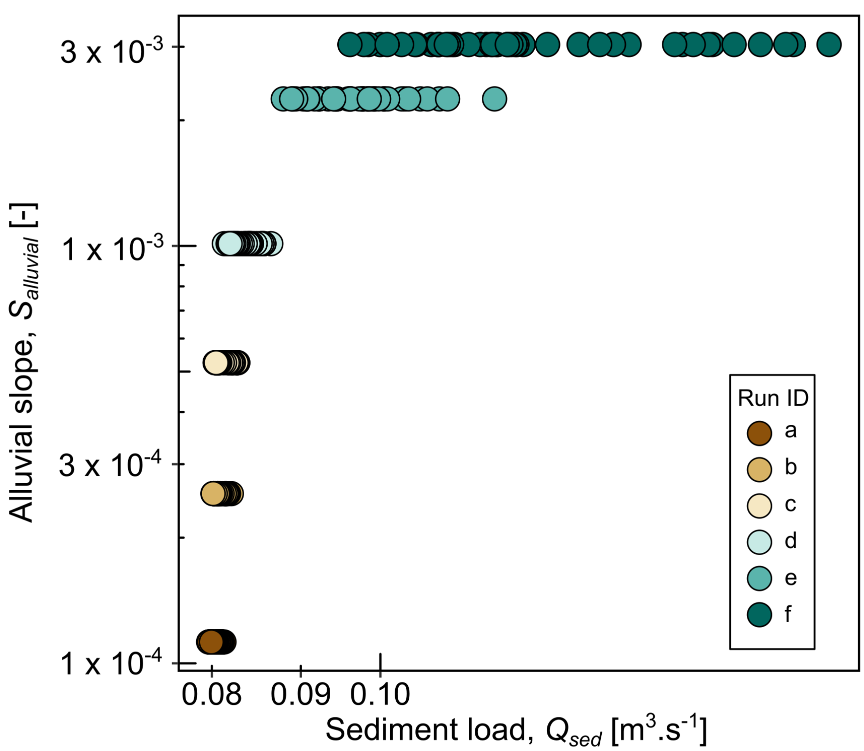
Alluvial slope, $S_{alluvial}$ [-]
Sediment load, Q_{sed} [m^3.s^{-1}]
Run ID
a
b
c
d
e
f

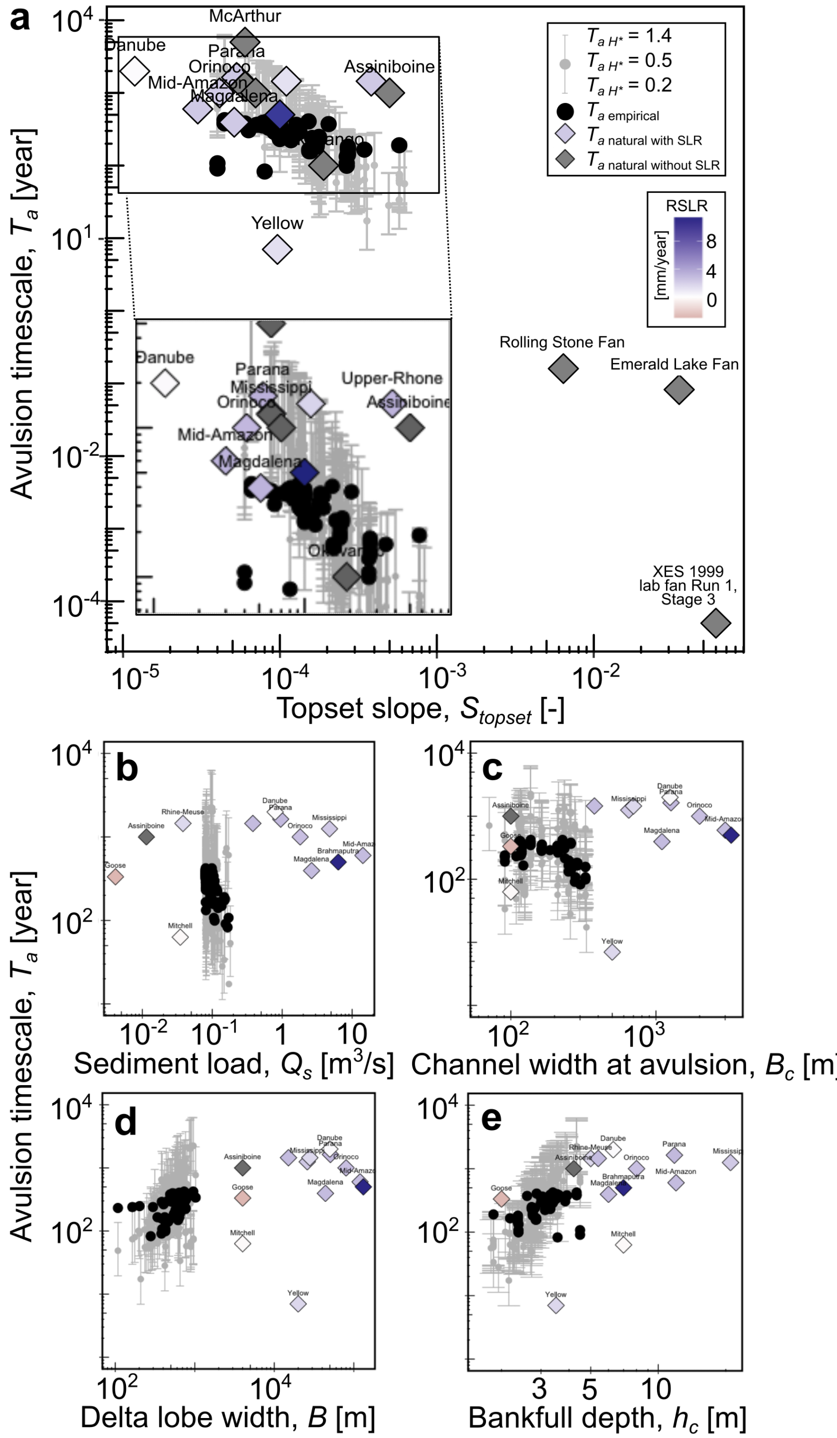

a
Avulsion timescale, T_a [year]
Topset slope, S_{topset} [-]
$T_{a\,H^*}$ = 1.4
$T_{a\,H^*}$ = 0.5
$T_{a\,H^*}$ = 0.2
T_a empirical
T_a natural with SLR
T_a natural without SLR
RSLR
[mm/year]
McArthur
Danube
Parana
Orinoco
Mid-Amazon
Magdalena
Assiniboine
Yellow
Mississippi
Upper-Rhone
Okavango
Rolling Stone Fan
Emerald Lake Fan
XES 1999
lab fan Run 1,
Stage 3
b
c
d
e
Sediment load, Q_s [m^3/s]
Channel width at avulsion, B_c [m]
Delta lobe width, B [m]
Bankfull depth, h_c [m]

First order controls of avulsion in river deltas

O.A. Prasojo[1*], T. B. Hoey[2], A. Owen[1] and R. D. Williams[1]

[1]*School of Geographical and Earth Sciences, University of Glasgow, University Avenue, Glasgow, G12 8QQ, United Kingdom, Octria.prasojo@glasgow.ac.uk, Amanda.Owen@glasgow.ac.uk, Richard.Williams@glasgow.ac.uk*

[2]*Department of Civil and Environmental Engineering, Brunel University London, Uxbridge, UB8 3PH, United Kingdom, Trevor.Hoey@brunel.ac.uk*

Highlights

- The dominant variables controlling the avulsion timescale in river deltas are investigated through a Delft3D numerical model
- Results show sediment load, controlled by alluvial slope upstream of a delta plain, serves as the first-order control of delta avulsion frequency
- This supports the hypothesis of upstream forcing controlling delta avulsion timescale and location, rather than downstream, backwater or sea-level rise, controls
- Comparison with an analytical solution, natural systems and laboratory deltas all show consistency with our numerical results

Abstract

Changed hydrological regimes, sea-level rise, and accelerated subsidence are all putting river deltas at risk across the globe. Deltas may respond to these stressors through the mechanism of avulsion. Decades of delta avulsion studies have resulted in conflicting hypotheses that avulsion frequency and location are upstream (water and sediment discharge) or downstream (backwater and sea-level rise) controlled. In this study, we use Delft3D morphodynamic simulations to investigate the main controls over delta avulsion. Avulsion timing and location were recorded in six scenarios modelled over a 400-year period with varying alluvial slopes upstream of a delta slope break ($1.13\text{x}10^{-4}$ to $3.04\text{x}10^{-3}$) within a range representative global deltas. We measure several independent morphometric variables including avulsion length, delta lobe width, channel width at avulsion, delta topset slope and sediment load. Correlating these variables with the avulsion timescales observed in our model shows that avulsion timescale is mostly controlled by sediment load, which in turn is controlled by the alluvial slope upstream of a delta slope break. With higher stream power index in steeper alluvial slopes, more sediment can be carried within a channel, resulting in more frequent avulsions. Our results are consistent with the avulsion timescale derived from an analytical solution, 19 natural deltas and downscaled physical laboratory deltas. These results help mitigate delta avulsion risk by focusing management efforts on variables that primarily control avulsion in a river delta, but also induce further debate over whether sea-level rise may, or may not, trigger more avulsions in river deltas.

Plain Language Summary

River deltas grow by distributing sediment along their channel courses into a sea or a lake. During river delta growth, channels can abruptly change course, which can cause devastating floods to people, infrastructure and landscapes. The timing and the processes associated with this channel course switching are currently debated. Using a computer model, we create virtual river deltas to understand how their networks of channels develop and switch during delta growth over a 400-year period. We find that the steeper the topography upstream of a river delta, the faster this abrupt change of channel course occurs. This is because steeper channels will erode and transport more sediment than less steep channels. Our model predictions of channel course timings are consistent with those observed from 19 natural river deltas. We now better understand the timing and the main cause of abrupt channel changes on deltas, a finding that aids flood risk management in river delta environments.

1. Introduction

River deltas are home for ~339 million people worldwide, are hotspots for biodiversity, and crucial carbon sinks (Ericson et al., 2006; Hackney et al., 2020; Loucks, 2019; Shields et al., 2017; Syvitski & Saito, 2007). However, the geomorphic dynamism of river deltas has been altered by growing stressors such as change in hydrologic regimes, sea-level rise, and accelerated subsidence, putting human and other systems that rely on river deltas at considerable risk (Giosan et al., 2014; Syvitski et al., 2009; Tessler et al., 2015; Wallace et al., 2014). One mechanism by which deltas respond to these stressors is by avulsing, which creates additional, or relocated, flood risk. Many studies have proposed controls over avulsion frequency in river deltas (e.g. Aslan et al., 2005; Brooke et al., 2020; Edmonds et al., 2009; Kleinhans & Hardy, 2013; Nijhuis et al., 2015; Slingerland & Smith, 2004) and avulsion location correlates with backwater length, avulsion length and valley exit point location (Ganti et al., 2016a; Hartley et al., 2017; Prasojo et al., 2022) but there is no consensus over which variable(s) is the most important factor contributing to delta avulsion frequency.

During avulsion, flow is abruptly diverted out of an established river channel into a new course on the adjacent floodplain or delta plain (Jones & Schumm, 2009; Slingerland & Smith, 2004). When a delta channel avulses, the population and economic activities on the delta plain can be placed at risk. Avulsions may be considered rare, but this is partly due to anthropogenic impacts and natural systems often exhibit avulsion over decadal timescales, for example on average once every 12 years in the Yellow River Delta (Jerolmack, 2009) or 4 years in Sulengguole River, China (Li et al., 2022). Different scales of avulsion have been recognised: full, where a new course completely leaves its parent channel; and, partial in which only a portion of the flow is diverted (McEwan et al., 2023). There are also several styles of avulsion: annexation in which a pre-existing channel is reoccupied; incision, where a new channel is scoured into the floodplain surface as a direct result of the avulsion; and, progradation, where extensive sediment deposition, such as a mouth bar, causes flow bifurcation and formation of a multi-channelled distributive network (Slingerland & Smith, 2004).

River deltas are initiated through repeated mouth bar deposition due to sudden expansion and deceleration of a sediment-laden jet of water entering relatively still water, usually a sea or lake (Bates, 1953; Edmonds et al., 2011; Kleinhans et al., 2013; Wright, 1977). Mouth bars grow in both upstream and downstream directions from the point of initiation, reach a height of c.0.4-0.6 of the initial flow depth, and stop growing once the sediment flux is advected around the mouth bar rather than accelerated over the bar (Edmonds & Slingerland, 2007; Fagherazzi et al., 2015; Kleinhans et al., 2013). This is the point where avulsion by progradation starts in a river delta. Simultaneously, avulsion by incision takes place in the proximal parts of a delta plain when mouth-bar deposition and stagnation induce parent channel backfilling or in-channel aggradation, triggering an avulsion to create a smaller distributive channel network by breaching the channel levee (Ganti et al., 2016a; Prasojo et al., 2022). The most upstream point where a delta channel starts to avulse is correlated with the location of a break in bed slope (Prasojo et al., 2022; Ratliff et al., 2021), the limit of the backwater zone (Brooke et al., 2022; Ganti et al., 2016a), or the exit point from the river valley (Hartley et al., 2017).

A strong correlation has been identified from 105 global river deltas between the locations of breaks in delta slope and avulsion nodes (Prasojo et al., 2022). Consequently, it is hypothesised that the slope of the alluvial river upstream of a delta controls the frequency of avulsion in the proximal parts of deltas, with steeper alluvial slopes leading to more frequent avulsions. This control is due to greater sediment transport capacity on steeper slopes (Bagnold, 1966). Hence, subject to sediment availability, steeper slopes transport more sediment per unit width into a delta plain. Assuming constant channel width, any reduction in energy slope across the delta plain leads to aggradation, the rate of which will be greater when upstream transport capacity is higher, which in turn leads to increased avulsion frequency (Jerolmack & Mohrig, 2007; Mohrig et al., 2000). Alternatively, lower alluvial slopes lead to lower sediment input rates and hence slower avulsion process.

To test this hypothesis, we use Delft3D morphodynamic simulation software to: 1) assess the effect of varying alluvial slopes upstream of a delta slope break on the avulsion timescale; and, 2) investigate what controls delta avulsion. Morphometric variables (delta lobe width, channel width at avulsion, avulsion length, topset slope, bankfull depth and sediment supply) were measured at every timestep during delta growth. These morphometric properties are considered to be independent variables that influence avulsion and so be correlated with avulsion timescales. This investigation aims to: (1) identify the first order controls of avulsion timescales from a suite of numerical model experiments with alluvial slope as the external forcing mechanism; (2) explain the mechanism of how the controlling variables control avulsion timescale; and, (3) compare the avulsion timescale from this numerical model to an analytical solution and natural river deltas. A robust understanding of these processes has practical implications due to their direct impact on coastal and inland flood risk on highly populated river deltas, as well as contributing to understanding of fundamental natural processes.

2. Methods

We designed a set of numerical experiments to model a natural scale river delta (7.5 x 7.5 km, 300 by 300 computational cells, each 625m^2) using Delft3D (v.4.04.02) software. We adopted physical parameters from the Delft3D river delta models from Edmonds & Slingerland (2010) and Caldwell & Edmonds (2014). Model bathymetry was designed to accommodate the six alluvial slopes defined below as our model scenarios.

2.1. Scenario definition

The model uses a range of alluvial slopes upstream of the delta's slope break ($S_{alluvial}$) (Fig. 1a), which are representative of natural river deltas (Fig. 1b). Ratios between $S_{alluvial}$ and downstream delta slopes (S_{DS}) measured from 105 global river deltas by Prasojo et al. (2022) were used to determine representative percentiles of this ratio (Fig. 1b; Table 1). Percentile 2.5 to 75 from $S_{alluvial}/S_{DS}$ ratio were used as our modelling scenario. These percentiles were then used to calculate model alluvial slopes using a constant initial downstream slope (S_{DS} = 0.000375) similar to that of the Atchafalaya Bay, Mississippi delta, Louisiana (Edmonds & Slingerland, 2010).

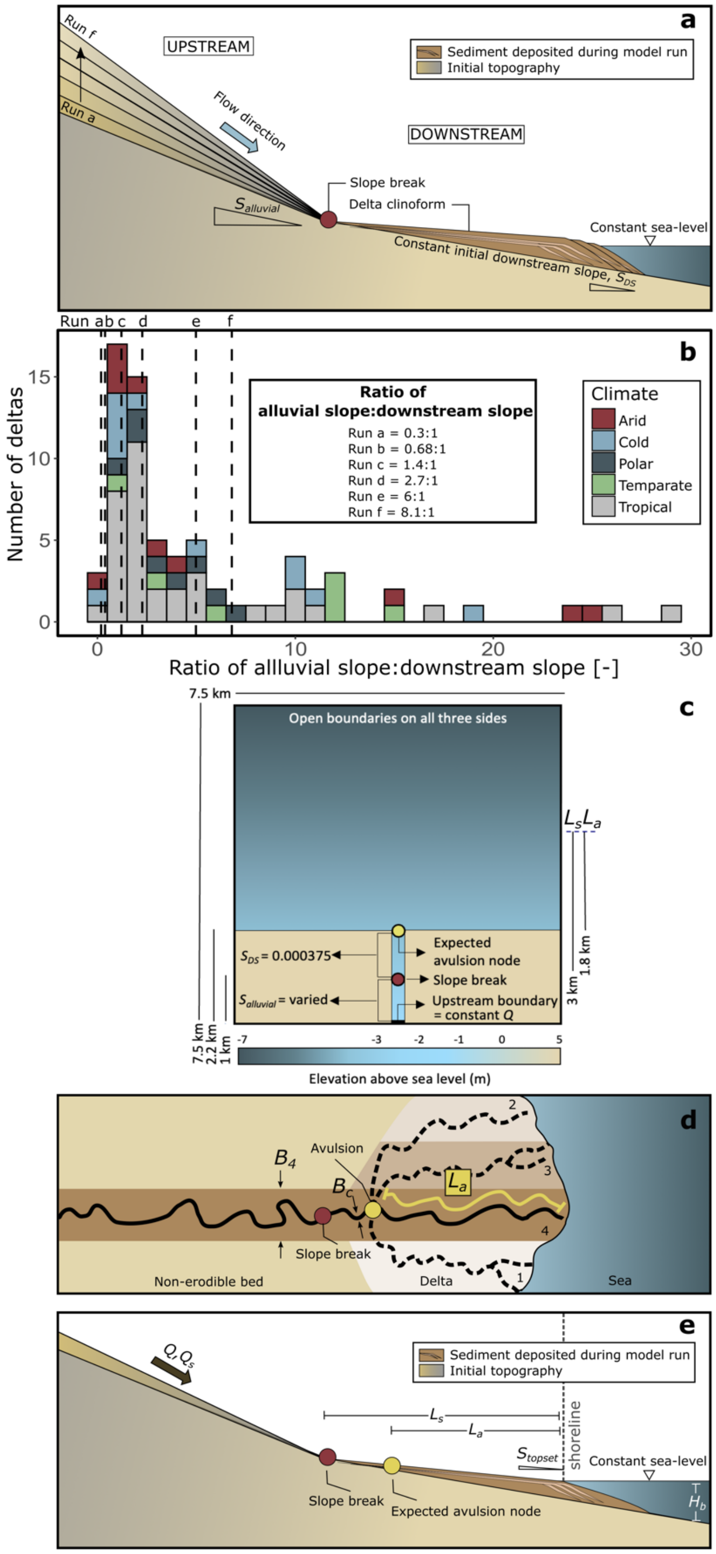

Figure 1. (a) Schematic diagram of the model design. The alluvial slope of each run was calculated from six percentiles from the alluvial slope-downstream slope ratios of modern river deltas shown in Fig. 1b. Initial downstream slope, S_{DS} is kept constant at 0.000375, the downstream slope of the modern Mississippi delta (Edmonds & Slingerland, 2010). (b) Distribution of the ratio between alluvial ($S_{alluvial}$) and downstream (S_{DS}) slopes from

105 modern river deltas distributed across five climate regions. Ratios used for numerical model runs are indicated by vertical dashed lines. (c) Plan view of the model design. L_s and L_a are slope break and avulsion lengths, respectively. The non-erodible bed at 5 m above sea level represents non-erodible bedrock. (d) Schematic diagram of a river delta showing avulsion location, inlet sediment supply (Q_s), lobe width of each avulsion (B), avulsion length (L_a) and channel widths measured at avulsion (B_c) modified from Chadwick et al. (2020). Numbers near the shoreline represent the number of delta lobes that were used to measure B; e.g. B_4 on (d) represents the width of the fourth lobe built. Schematic cross-section showing basin depth (H_b) and topset slope (S_{topset}). Parameters shown in Fig. 1d-e are measured at each timestep during delta growth.

2.2. Model setup

We use Delft3D software to model six scenarios. Delft3D is a physics-based model that simulates hydrodynamics and morphodynamics (Edmonds & Slingerland, 2010; Caldwell & Edmonds, 2014; Nienhuis et al., 2018a;b) and has been validated for a wide range of environments, including self-formed river deltas (Edmonds & Slingerland, 2007, 2008; Geleynse et al., 2011; Morgan et al., 2020; Nijhuis et al., 2015; Rossi et al., 2016; Williams et al., 2016). Flow is computed using depth-averaged, nonlinear, shallow-water equations obtained from three-dimensional Reynolds-averaged Navier-Stokes equations (Edmonds & Slingerland, 2010). The modelled velocity distribution is then used to compute sediment transport (only suspended load is applied in our model) and to update the bed elevation according to divergence in sediment transport (Caldwell & Edmonds, 2014).

Table 1. Numerical modelling scenarios as defined in Fig. 1.

Run ID	Percentile from $S_{alluvial}$ to S_{DS} ratio	Alluvial slope, $S_{alluvial}$	Initial downstream slope, S_{DS}	Ratio of alluvial slope to downstream slope
a	2.5	1.13×10^{-4}	3.75×10^{-4}	0.3
b	10	2.55×10^{-4}	3.75×10^{-4}	0.68
c	25	5.25×10^{-4}	3.75×10^{-4}	1.4
d	50	1.01×10^{-3}	3.75×10^{-4}	2.7
e	71	2.25×10^{-3}	3.75×10^{-4}	6.0
f	75	3.04×10^{-3}	3.75×10^{-4}	8.1

We adopted physical parameters from a previous synthetic self-formed river delta numerical model ('scenario o') from Edmonds & Slingerland (2010) and Caldwell & Edmonds (2014) (Fig. 1c). The model is rectangular with four boundaries, the incoming river discharge being located at the 'South' boundary of the model and the other three boundaries set to 0 m elevation above sea level (Fig. 1c). The constant incoming river discharge, set at 1050 $m^3.s^{-1}$, is uniformly distributed across the 250 m wide inlet channel, and inlet sediment discharge is in equilibrium with transport capacity. Various alluvial slopes are achieved by having various inlet channel bathymetry in each run while maintaining the receiving basin's bathymetry. Our modelled deltas closely represent natural deltas because the discharge ratio and the differences in bed heights between bifurcating distributary channels follow similar ranges reported for natural deltas (Edmonds & Slingerland, 2010). Sea-level remains constant within the model, and no tide or wave effects are considered.

The model domain is 7.5 km x 7.5 km to avoid the delta plain extending across the model boundaries. We introduce a slope break 1 km from the inlet boundary to drive delta formation in the model's initial bathymetry. Using the slope break-avulsion length scaling identified from global river deltas (Prasojo et al., 2022) the expected avulsion node location should emerge in each scenario at around 2.2 km from the inlet (Fig.1c). A constant sediment grain-size distribution is used throughout the model (D_{50} = 125μm with a normal Gaussian distribution, medium-grain silt D_{50} = 30μm is introduced as cohesive sediment), the critical bed shear stress for erosion = 0.10 $N.m^{-2}$, and the model begins with 5 metres of fully mixed sediment. Other physical and numerical parameters were held constant across all scenarios (Table 2).

During an 18 days simulation, the model produces one output every 480 minutes. Hence at the end of simulation, the model stores 52 visualisation outputs (i.e. maps). Using a morphological scale factor (*morfac*) of 175, these 52 maps represent 3150 days (8.6 years) of prototype time with constant input discharge. Because bankfull discharge occurs for c.2% of time on average, 18 days of simulation thus represents around 430 years of 'real' time (i.e. 8.6 years divided by 0.02).

Table 2. User-defined model parameters (adopted from Edmonds & Slingerland (2010); Caldwell & Edmonds (2014)).

Parameter	Value	Units
Grid size	300 x 300	cells
	7.5 x 7.5	km
Cell size	25 x 25	m
Run duration	18	days
Basin bed slope (downstream of slope break)	0.000375	(-)
Initial channel dimension (width x depth)	250 x 2.5	m
Upstream non-erodible bed elevation	5	m
Initial channel length upstream of slope break	1000	m
Initial avulsion length from the expected shoreline	1800	m
Water discharge	1050	$m^3.s^{-1}$
Constant water surface elevation at downstream open boundary	0	m
Initial sediment layer thickness at bed	5	m
Number of subsurface stratigraphy bed layers	1	(-)
Computational time step	0.2	min
Output interval	480	min
Morphological scale factor	175	(-)
Spin-up interval	720	min

2.3. Surface metric

When the model reaches an equilibrium (i.e. model's inlet shows constant sediment discharge and channel depth at timestep > 200 years), we begin the morphometric and avulsion timescale measurement. Avulsions throughout 18 days of simulation were empirically observed at the expected avulsion node location (Fig. 1c) or at the 'valley exit' in which an inlet channel meets the open water in the model. Avulsion in the model is defined when a distributive channel produced during delta formation changes its course and deposits a new delta lobe. Hence, we limit our avulsion observations to those caused by progradation or incision and not by annexation, which may occur on the more distal delta plain (Slingerland & Smith, 2004). Consequently, only the most upstream avulsions are observed in this study. Every time avulsion is observed in the model, computational timescale is noted and converted to a 'real' time as $T_{a\ \mathrm{empirical}}$.

Measured surface metrics are adopted from an analytical solution for avulsion timescale as a function of delta lobe width (B), channel width at avulsion (B_c), avulsion length (L_a), basin depth (H_b), magnitude of relative sea-level rise (z), topset slope (S_{topset}), bankfull depth (h_c) and sediment supply (Q_s) (Eq. 4 from Chadwick et al., 2020). Avulsion length, delta lobe width, channel width at avulsion and delta topset slope were measured over 52 maps. The delta lobe width (B), channel width at each avulsion node (B_c) and avulsion length (L_a) were measured in QGIS from the georeferenced images produced by Delft3D (Fig. 1d, Table S1). Delta lobe width (B) is measured as the maximum width of each lobe, while avulsion length (L_a) is measured along the longest channel from the shoreline to the most upstream avulsion node located at the 'expected avulsion node' mentioned in Fig. 1c. Topset slope (S_{topset}) was calculated by linear regression through topset elevations along a longitudinal cross-section located through the centre of the model from the delta shoreline to the delta slope break introduced in the model (i.e. located 1 km from the model's South boundary) (Fig. 1e). Sediment supply (Q_s) at the channel inlet was obtained from a Delft3D visualisation software, QUICKPLOT (v2.60.65942).

Bankfull depth (h_c) was calculated using Eq. 1 (Parker, 2004).

$$h_c = \left(\frac{C_f Q^2}{g {B_c}^2 S_{topset}}\right)^{\frac{1}{3}} \tag{1}$$

C_f is defined as bed friction coefficient [-] = 0.002 for large lowland rivers (Parker et al., 2007), Q = bankfull discharge [$m^3.s^{-1}$] = 1050 $m^3.s^{-1}$, g = gravitational acceleration [$m.s^{-2}$] = 9.81 $m.s^{-2}$, B_c = channel width at avulsion node [m], and finally S_{topset} = topset slope [-].

The avulsion timescale empirically observed at each time an avulsion occurred ($T_{a\ empirical}$) was correlated with all the measured morphometric variables (e.g. Q_s, L_a, B_c, B, S_{topset}, $S_{alluvial}$, and h_c) from all 52 maps. Scatter plots and Pearson correlation coefficients (r) were used to assess the linearity of relationships and potential dependencies between all variables.

3. Results

Fig. 2 shows the morphology of the deltas in each scenario at the final timestep. Overall, the different alluvial slopes produce delta plains that exhibit different shoreline configurations, different numbers of active distributary channels and slightly different delta plain sizes. One delta plain reached the model boundary (Run f) and this scenario was repeated with a larger domain size (Fig. S1) and the avulsion timescales were observed from this larger domain.

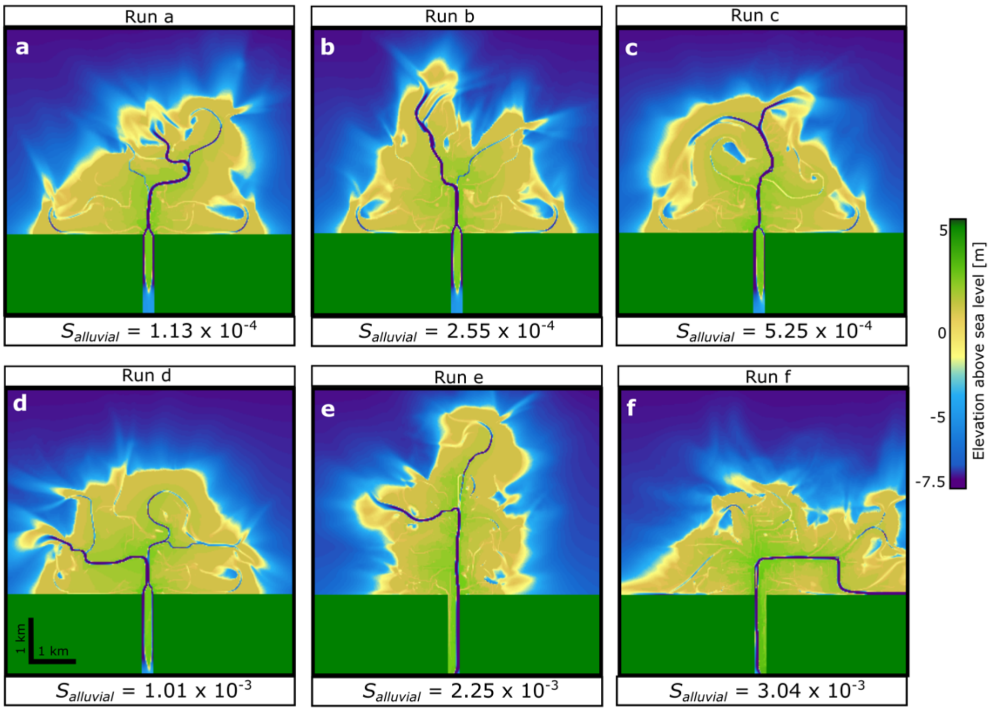

Figure 2. (a-f) River deltas for each run at the final simulation timestep. *Run f* was repeated with a larger (12.5 x 12.5 km) model size (Fig. S1) to avoid the delta plain reaching the model's boundary. Morphometric measurements for Run f were made on this larger model size.

Avulsion timescale observed in the model occurs as quickly as 82.7 years with the longest of 428 years after the model starts. Skewed distribution of avulsion timescale can be observed in most scenario runs (Fig. S2) with overall median value of 297.7 years and mean value of 278.9 years. Run a and b do not show significant difference in avulsion timescale range. However, later runs show a decrease of avulsion timescale as the median value of avulsion timescale was found to be 340 years in run c, in contrast to 175 years in run f (Fig. S2).

Fig. 3 shows correlations between observed avulsion timescales in the model ($T_{a\ empirical}$) and the independent morphometric variables measured in each timestep and relationships between those independent variables. $T_{a\ empirical}$ has a high correlation with sediment supply, Q_s (r = -0.62; p = 6.76 x 10^{-10}). $T_{a\ empirical}$ is also correlated with channel width at avulsion (B_c; r = -0.56, p = 1.76 x 10^{-6}), topset slope (S_{topset}; r = -0.54; p =1.4 x 10^{-4}), delta lobe width (B; r = 0.51, p = 1.74 x 10^{-4}), alluvial slope ($S_{alluvial}$; r = -0.48, p = 8.45 x 10^{-4}), bankfull depth (h_c; r = 0.48; p = 1.38 x 10^{-4}) and avulsion length (L_a; r = 0.4, p = 2.18 x 10^{-4}).

Sediment load (Q_s) is driven by the alluvial slope ($S_{alluvial}$) that is independently defined in the model (Fig. 1a), leading to a correlation r = 0.8 between these variables (Fig. 3). A morphological consequence of sediment load is that bankfull depth (h_c) is highly correlated (r = -0.86) with topset slope (S_{topset}) as defined from Eq. 1. Moderate correlations are found between other morphometric variables, such as B_c-B, B_c-L_a, B-L_a, $S_{alluvial}$-L_a, because as a delta grows the delta plain and its' constituent channels and islands enlarge in an allometric manner, as observed in natural, physical laboratory and numerical deltas (Wolinsky et al., 2010). Additionally, alluvial slope seems to control the avulsion length (r = 0.65, p < 2.2 x 10^{-16}), consistent with the findings from a survey of global river deltas (Prasojo et al., 2022).

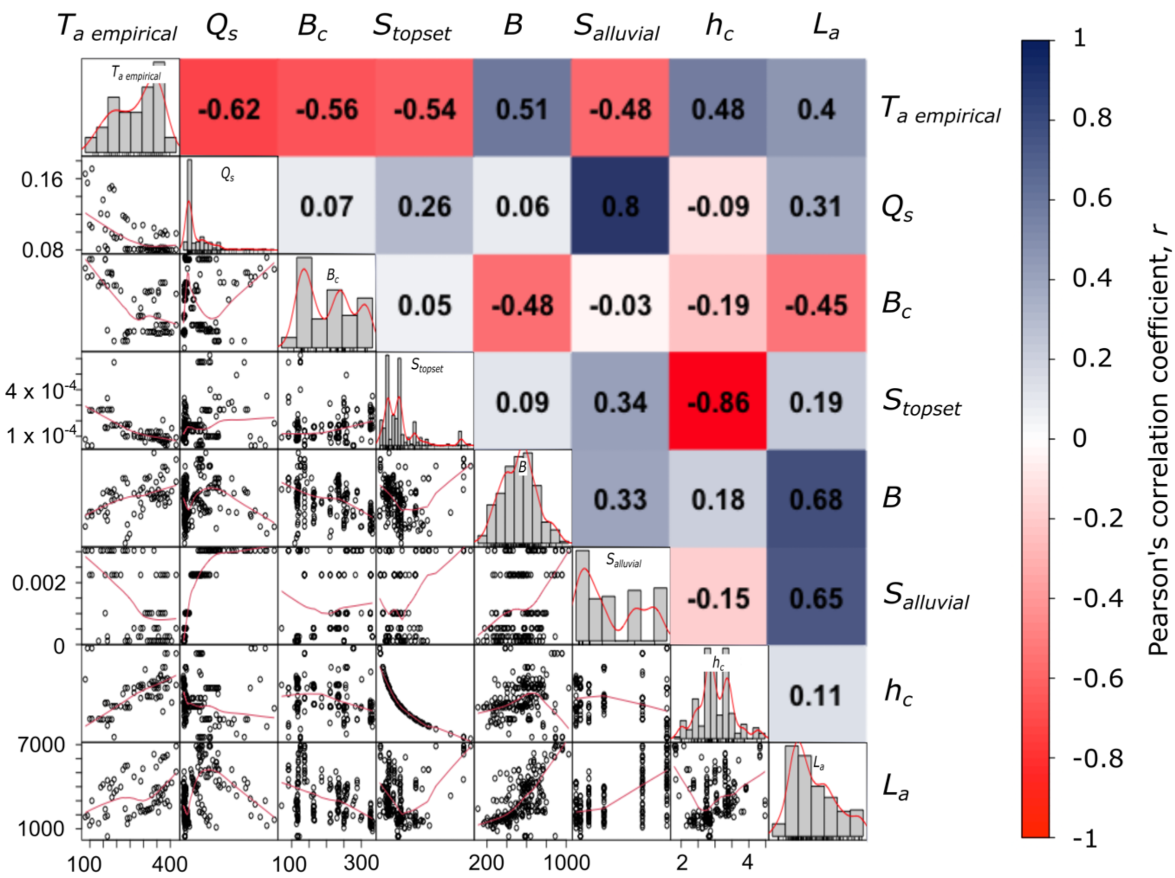

Figure 3. Pearson correlations between avulsion timestep ($T_{a\ empirical}$) and independent morphometric variables with N = 233 along with their distributions and correlations. Units on this figure are years for $T_{a\ \mathrm{empirical}}$, $m^3.s^{-1}$ for Q_s, meters for B_c, h_c and L_a, consecutively. S_{topset} and $S_{alluvial}$ are dimensionless. Note that h_c is autocorrelated with S_{topset} as shown in Eq. 1.

Fig. 4 shows the data from the model and ordinary least square regressions for the highest correlations in Fig. 3. The regression relationships are statistically significant and have narrow confidence bands (grey shaded areas in Fig. 4), although the data exhibit scatter and some clustering. Avulsion timescale is inversely correlated with sediment load (Fig. 4a), which may reflect high aggradation rates when sediment loads are greater. This process link becomes more apparent when considering topset slope (Fig. 4b) which is a consequence of sediment load and aggradation. The correlation between channel width and slope that results from flow energy in turn produces a negative relationship between avulsion timescale and channel width at the avulsion location (Fig. 4c). Avulsion timescales increase with the size of the delta, represented by lobe width (Fig. 4d), bankfull depth (Fig. 4e) and avulsion length (Fig. 4f). Both lobe width and avulsion length plots contain separate clusters of data points that may indicate alternative patterns of morphological adjustment. The weak positive correlation between avulsion length and timescale challenges the hypothesis that backwater length controls avulsion timescale (Chadwick et al., 2020; Chatanantavet et al., 2012; Ganti et al., 2016a,b).

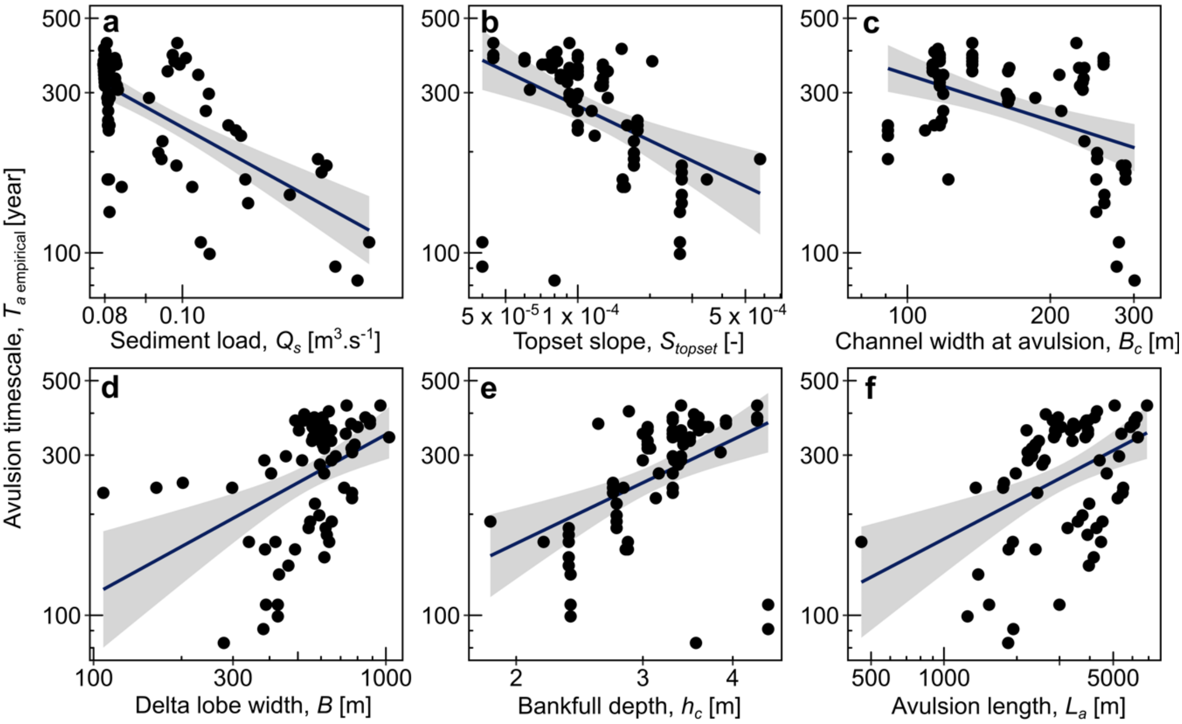

$T_{a\ empirical} = 11.45Q_s^{-1.32}$, $R^2 = 0.38$, $p = 6.76 \times 10^{-10}$, $SE_{residual} = 0.32$
$T_{a\ empirical} = 11.7S_{topset}^{-0.34}$, $R^2 = 0.23$, $p = 1.4 \times 10^{-4}$, $SE_{residual} = 0.38$
$T_{a\ empirical} = 4572.6B_c^{-0.56}$, $R^2 = 0.21$, $p = 1.76 \times 10^{-6}$, $SE_{residual} = 0.32$
$T_{a\ empirical} = 12.77B^{0.48}$, $R^2 = 0.24$, $p = 1.74 \times 10^{-4}$, $SE_{residual} = 0.38$
$T_{a\ empirical} = 80.34h_c^{1.03}$, $R^2 = 0.23$, $p = 1.38 \times 10^{-4}$, $SE_{residual} = 0.38$
$T_{a\ empirical} = 12.45L_a^{0.38}$, $R^2 = 0.18$, $p = 2.18 \times 10^{-4}$, $SE_{residual} = 0.38$

Figure 4. Regressions of independent morphometric variables against avulsion timescale ($T_{a\ empirical}$) observed in model runs with 95% confidence band in grey (N = 233). Note that data exhibit scatter and some clustering (a,d) that may indicate alternative patterns of morphological adjustment.

4. Discussion

The six scenarios used in this study provide insight into avulsion processes from the inception of delta building. Since avulsion is infrequent, it is difficult to acquire large data sets from field studies. By observing avulsions in a numerical river delta model, we can generate a large data set from which to infer the process controls over avulsion timescales.

4.1. Investigating the first-order controls of avulsion timescales

Sediment load (Q_s) has a high correlation with avulsion timescale observed in the model ($T_{a\ empirical}$) (Figs. 3,4) and Q_s is controlled by the imposed alluvial slope ($S_{alluvial}$) (Table 3, Fig. 5). Higher alluvial slopes and sediment loads (Q_s) increase the vertical aggradation rate (v_a) in the proximal part of the delta leading to increased topset slopes (Chadwick et al., 2020). Since avulsion timescale is proportional to the rate of vertical aggradation (Jerolmack & Mohrig, 2007; Mohrig et al., 2000), higher vertical aggradation rates lead to the more frequent avulsions. Hence the avulsion timescale in our model is controlled by the alluvial slope that was defined independently in our scenarios. This sediment mass-balance approach to understanding avulsion timescales has been used in analytical solutions including a radially averaged model (Muto, 2001; Muto & Steel, 1997), a channel-averaged model (Reitz et al., 2010), and backwater-scaled models (Chadwick et al., 2019; Moodie et al., 2019).

Table 3. Cumulative sediment load and median avulsion timescale produced from each scenario. The median avulsion timescale is used to better represent the skewed distribution of avulsion timescale (Fig. 3).

Run ID	Alluvial slope, $S_{alluvial}$	Cumulative sediment load, ΣQ_{sed} [$m^3.s^{-1}$]	Median avulsion timescale, $T_{a\ median}$ [year]
a	1.13×10^{-4}	2.98	335.0
b	2.55×10^{-4}	3.07	322.5
c	5.25×10^{-4}	2.85	339.1
d	1.01×10^{-3}	3.09	330.8
e	2.25×10^{-3}	4.09	252.2
f	3.04×10^{-3}	5.47	181.9

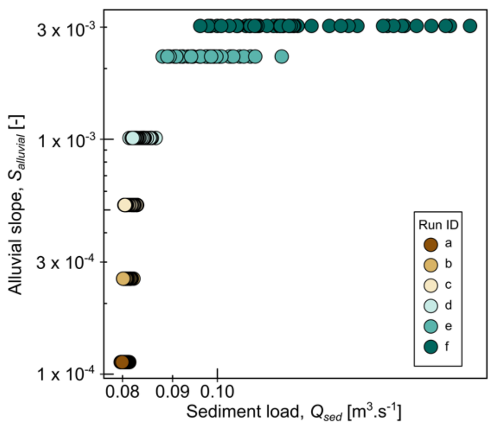

Figure 5. Relationship between sediment load (Q_{sed}) and alluvial slopes ($S_{alluvial}$) imposed to each scenario.

In this study we show how, with a constant sea-level boundary condition, top-down forcing of alluvial slope controls the likelihood for a channel to aggrade and then avulse most of its water and sediment into a new channel or the surrounding delta plain. This finding is consistent with a conceptual model of slope break-avulsion length scaling derived from a database of global river deltas by Prasojo et al. (2022). They suggested that this scaling implies that the slope break is the prevalent driver of avulsion rather than bottom-up control from backwater length or sea-level rise (Chadwick et al., 2020; Chatanantavet et al., 2012; Ganti et al., 2016b). In our model, varied in-channel aggradation due to the imposed alluvial slope acts as the dominant trigger for avulsion. This reasoning is corroborated by a numerical model in which the location of avulsion node consistently scales with the slope break due to linear diffusion of aggradation and erosion of the riverbed, even under sea-level rise (Ratliff et al., 2021).

4.2. Comparison with analytical solution and natural deltas

Chadwick et al's (2020) mass-balance based analytical solution is used to calculate expected avulsion timescales for our model conditions (Eqs. 3-6, Table S1). Measured independent morphometric variables are used in Eqs. 3-6 to calculate avulsion frequency (f_a) and timescale (T_a).

$$f_a = \frac{1}{T_a} = \frac{1}{(1-\lambda_p)} \frac{Q_s}{(L_a - D)BH + DB\left(H_b + z + \frac{DS_{topset}}{2}\right)} \; if \; D \geq 0 \tag{3}$$

$$f_a = \frac{1}{T_a} = \frac{1}{(1-\lambda_p)} \frac{Q_s}{L_a BH} \; if \; D < 0 \tag{4}$$

$$D = (H - z)/S_{topset} \tag{5}$$

$$H = H^{*} h_c \tag{6}$$

with f_a = avulsion frequency [year^{-1}], Q_s = sediment load [m^3.s^{-1}], λ_p = sediment porosity [-], L_a = avulsion length [m], D = delta lobe-progradation distance [km], B = delta lobe width of each avulsion [m], H = aggradation thickness necessary for avulsion [m], H_b = basin depth [m], z = magnitude of sea level rise [m], S_{topset} = topset slope [-], H^* = avulsion threshold [-], and h_c = bankfull depth [m] calculated using Eq. 1.

In calculating these analytical avulsion timescales, sensitivity analyses were undertaken using avulsion thresholds (H^*) of 0.2, 0.5, and 1.4, which are realistic for lowland deltas (Ganti et al., 2019), and D > 0 since there is no allogenic forcing that would make the delta regress. The analytical avulsion timescales for H^* = 0.2, 0.5, and 1.4 are $T_{a\ H^* = 0.2}$, $T_{a\ H^* = 0.5}$, and $T_{a\ H^* = 1.4}$, respectively (Table S1). Since sea-level is constant in this study, sea level rise, z = 0. Sediment porosity (λ_p) is assumed to be 0.4 (Jerolmack, 2009; Paola et al., 2011), bed friction coefficient (C_f) = 0.002 for lowland rivers (Parker et al., 2007), and constant bankfull discharge (Q) = 1050 m^3.s^{-1}.

Analytical avulsion timescales were then compared to avulsion timescales observed from 19 natural river deltas, two fan deltas and one downscaled physical laboratory fan delta mentioned in Chadwick et al. (2020) and Jerolmack & Mohrig (2007), using topset slope values from Prasojo et al. (2022) (Table S2). Fig. 6 shows how avulsion timescales observed in our model fit both the pattern and the magnitude of both the analytical solution and natural delta observations when correlated with topset slope (S_{topset}) (Fig. 6a), sediment load (Q_s) (Fig. 6b), channel width at avulsion (B_c) (Fig. 6c), delta lobe width (B) (Fig. 6d) and bankfull depth (h_c) (Fig. 6e).

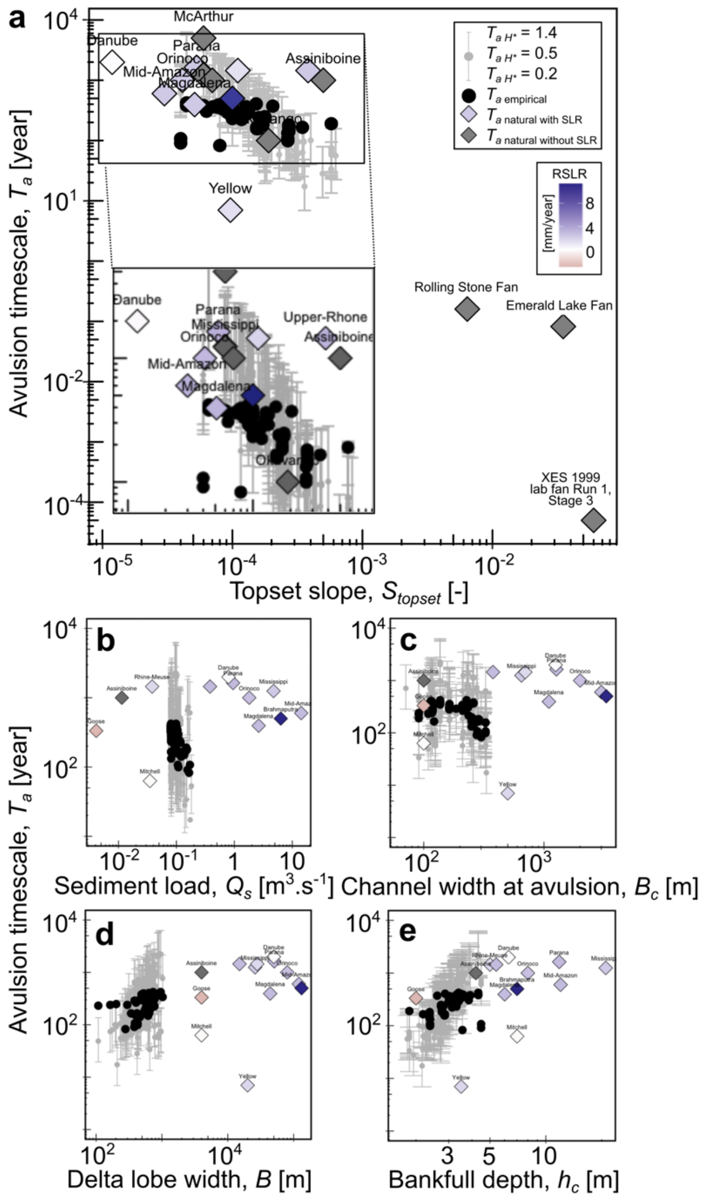

Figure 6. Relationships between avulsion timescales and independent variables: (a) topset slope with inset showing a more detail plot; (b) total sediment load; (c) channel width at the avulsion location; (d) delta lobe width; and, (e) bankfull channel depth from model, analytical equations and natural deltas. The plots show model values ($T_{a\ empirical}$) and those calculated from analytical equations (eqs. 3-6). Solid black circles are empirical results from the model. Grey dots and bars are results from the analytical equations using three avulsion threshold H^* values ($T_{a\ H^* = 1.4}$, $T_{a\ H^* = 0.5}$, $T_{a\ H^* = 0.2}$). Diamonds are results from the analytical equations applied to natural and laboratory deltas: grey diamonds have constant sea-level; purple diamonds are for deltas with relative sea-level rise ($RSLR$; mm.yr^{-1}) colour-coded as shown. Data from natural deltas and the laboratory experiment are available in Table S2.

In contrast, the avulsion timescales calculated for natural deltas ($T_{a\ natural}$) are not correlated with relative sea-level rise rate ($RSLR$) (Fig. 6a and Fig. S3). This result supports the hypothesis that the location of avulsions is unaffected by sea-level rise, as also found in an earlier numerical model study (Ratliff et al., 2021). Avulsion location is thus controlled by upstream forcing (alluvial slope) (Prasojo et al., 2022) rather than downstream forcing by sea-level rise or backwater influence (Chadwick et al., 2020; Chatanantavet et al., 2012; Ganti et al., 2016b). As in our previous field-based empirical study (Prasojo et al., 2022), these results demonstrate that total sediment load, controlled by alluvial slope upstream of a delta slope break, has a more dominant role in defining delta avulsion frequency than does sea-level. Alluvial channels may increase their sediment transport capacity through width adjustment, leading to the observed correlation between channel width and avulsion timescale (Fig. 6c). This consequently raises the question as to whether *RSLR* may lead to increased avulsion frequency in river deltas.

Previous literature on the relationship between the frequency of avulsion and sea-level rise is equivocal. A field study conducted in Mitchell River delta, Australia found that avulsion frequency increases with sea-level fall (Lane et al., 2017). Numerical model results suggest that avulsions on the Mississippi (faster) and Trinity (slower) Rivers showed different responses to Holocene sea-level rise even though they are geographically adjacent (Chatanantavet et al., 2012; Moran et al., 2017). An example during sea-level fall from the Goose River delta, Canada, shows that avulsion frequency remained constant during this base-level adjustment (Nijhuis et al., 2015). In contrast, avulsion frequency in the Rhine-Meuse delta, Netherlands, increased during the Holocene sea-level rise period (Törnqvist, 1994), possibly due to aggradation rate (Q_s) being controlled by *RSLR*. However, we do not find Q_s-*RSLR* relationship in the 19 natural deltas reported in this study (Fig. S4).

Overall, these previous studies and our results (Fig. 6) imply that while the frequency of the most upstream avulsion on a delta is controlled by upstream sediment supply, the frequency of more distal avulsions has an unclear relationship with either upstream controls or the rate of relative sea-level change. Further investigation from numerical models, analytical models and/or field data is needed to resolve this issue.

4.3. Implications for delta management

Our modelling results advance our understanding about how alluvial slope, which controls sediment load input, regulates the most upstream avulsion location and timescale. Note that the avulsion analysed in this modelling study is the most upstream avulsion node associated with the slope break and/or valley exit (Fig. 1c) and not avulsion nodes located further downstream the delta plain. The complex hydraulic and sediment transport processes that deliver these correlations are linked to aggradation rate and hence topset slope. Consequently, with the increase of anthropogenic forcing both directly within river deltas and throughout upstream catchment areas (Best, 2019; Darby et al., 2015; Dunn et al., 2019; Hackney et al., 2020), delta managers can use sediment load management to reduce the risk of avulsion driven flooding. Interventions that control sediment load may be more effective than those which address other less dominant factors such as flood variability, delta size, or channel morphology (Aslan et al., 2005; Brooke et al., 2020; Edmonds et al., 2009; Nienhuis et al., 2018; Slingerland & Smith, 2004; Valenza et al., 2020).

However, finding a perfect balance between maintaining sediment load to nourish delta environments and to hinder deltas' risk to coastal erosion is challenging. Current deforestation rate increases sediment supply, responsible for 25% of delta net land gain, but also hastening the next avulsion (Nienhuis et al., 2020). Alternatively, river damming is responsible for more than 50% reduction in sediment delivery, collectively leading to a loss of a delta land of 12 km^2 annually (Nienhuis et al., 2020). This declining sediment load not only poses threats to the long-term sustainability of deltas but also renders them susceptible to adverse effects from rising sea levels, sand mining and ecological degradation due to sediment starvation (Jordan et al., 2019). Therefore, gaining insights into the distribution patterns and quantities of sediments in the delta is imperative to ensure its continued sustainability.

4.4. Next steps

An important extension of this modelling work is to vary water discharge (*Q*) and sediment load (Q_s) as variability in these may affect the geomorphic processes controlling avulsion timescale. Multi-temporal observation of well-studied natural river deltas, such as the Yellow (Moodie et al., 2019), Mississippi (Chamberlain et al., 2018) or Rhine-Meuse (Pierik et al., 2018; Stouthamer et al., 2015) deltas, could then be used to validate model results. Moreover, incorporating other variables such as grain size and sediment cohesion, forcing through sea-level rise and subsidence, and adding vegetation that controls crevassing and consequently increases avulsion timescale in future numerical modelling should be considered (Nienhuis et al., 2018; Pierik et al., 2023; Sanks et al., 2022). In particular, considering the importance of projected global sea-level changes and the variability of results reported in the literature, better understanding of sea-level rise impacts on delta avulsion is needed.

We have used a simplified modelling approach and have isolated one controlling variable while holding other factors constant. Observations of the processes and evolution in the numerical deltas shows the complexity of hydraulic and morphodynamic processes across delta plains. Future work will need to address this complexity, including: (a) How does the forcing studied here (alluvial slope) interact with a combination of other factors (e.g. sea-level, wave and tidal regimes, and anthropogenic effects)? (b) How do the other controls (e.g. Q_s, *Q*, riverbank material, vegetation) in river deltas influence avulsion timescales? And, (c) how might these avulsion signals be preserved or shredded in the rock record?

5. Conclusion

We conducted a suite of numerical morphodynamic modelling experiments with variable river alluvial slopes (from 1.13×10^{-4} to 3.04×10^{-3}) to understand the controls over avulsion location and timescale in a river delta. Sediment load, which is directly driven by alluvial slope, is the dominant control of the timescale of avulsion. Mechanistically, this is due to greater sediment transport capacity over steeper alluvial slopes leading to increased sediment input to the delta plain, accelerated vertical aggradation and more frequent avulsion. The results support the hypothesis of upstream forcing controlling delta avulsion timescale and location, rather than downstream controls by backwater length or sea-level rise. A robust understanding of the main factors controlling avulsion in river deltas has significant implications due to their direct impacts on (i) coastal and inland hazards on highly populated river deltas and (ii) rock record interpretation.

Acknowledgements

This study was funded by an Indonesia Endowment Fund for Education (LPDP) awarded to Prasojo. We also thank A.J.F. (Ton) Hoitink, Andrew Moodie and other referees of an earlier version who have contributed significantly to improve the quality of this manuscript.

Open Research

The morphometric variables and avulsion timescales observed from our models are available in Table S1. The dataset from natural and laboratory river deltas used in this study (Table S2) and model scenarios (Run a-f) are available in the FigShare repository (Prasojo et al., 2023a,b).

References

Aslan, A., Autin, W. J., & Blum, M. D. (2005). Causes of river avulsion: Insights from the late Holocene avulsion history of the Mississippi River, U.S.A. *Journal of Sedimentary Research*, *75*(4), 650–664. https://doi.org/10.2110/jsr.2005.053

Bagnold, R. A. (n.d.). *An Approach to the Sediment Transport Problem From General Physics*. Retrieved from doi:10.3133/pp422i

Bates, C. C. (1953). Rational Theory of Delta Formation. *AAPG Bulletin*, *37*(9), 2119–2162. https://doi.org/10.1306/5ceadd76-16bb-11d7-8645000102c1865d

Best, J. (2019). Anthropogenic stresses on the world's big rivers. *Nature Geoscience*, *12*(1), 7–21. https://doi.org/10.1038/s41561-018-0262-x

Brooke, S., Chadwick, A. J., Silvestre, J., Lamb, M. P., Edmonds, D. A., & Ganti, V. (2022). Where rivers jump course. *Science*, *376*(6596), 2023. https://doi.org/10.1126/SCIENCE.ABM1215/SUPPL_FILE/SCIENCE.ABM1215_MOVIES_S1_AND_S2.ZIP

Brooke, Sam, Ganti, V., Chadwick, A. J., & Lamb, M. P. (2020). Flood Variability Determines the Location of Lobe-Scale Avulsions on Deltas: Madagascar. *Geophysical Research Letters*, *47*(20), e2020GL088797. https://doi.org/10.1029/2020GL088797

Caldwell, R. L., & Edmonds, D. A. (2014). The effects of sediment properties on deltaic processes and morphologies: A numerical modeling study. *Journal of Geophysical Research: Earth Surface*, *119*(5), 961–982. https://doi.org/10.1002/2013JF002965

Chadwick, A. J., Lamb, M. P., Moodie, A. J., Parker, G., & Nittrouer, J. A. (2019). Origin of a Preferential Avulsion Node on Lowland River Deltas. *Geophysical Research Letters*, *46*(8), 4267–4277. https://doi.org/10.1029/2019GL082491

Chadwick, A. J., Lamb, M. P., & Ganti, V. (2020). Accelerated river avulsion frequency on lowland deltas due to sea-level rise. *Proceedings of the National Academy of Sciences of the United States of America*, *117*(30), 17584–17590. https://doi.org/10.1073/pnas.1912351117

Chatanantavet, P., Lamb, M. P., & Nittrouer, J. A. (2012). Backwater controls of avulsion location on deltas. *Geophysical Research Letters*, *39*(1), 2–7. https://doi.org/10.1029/2011GL050197

Darby, S. E., Dunn, F. E., Nicholls, R. J., Rahman, M., & Riddy, L. (2015). A first look at the influence of anthropogenic climate change on the future delivery of fluvial sediment to the Ganges–Brahmaputra–Meghna delta. *Environmental Science: Processes & Impacts*, *17*(9), 1587–1600. https://doi.org/10.1039/C5EM00252D

Dunn, F. E., Darby, S. E., Nicholls, R. J., Cohen, S., Zarfl, C., & Fekete, B. M. (2019). Projections of declining fluvial sediment delivery to major deltas worldwide in response to climate change and anthropogenic stress. *Environmental Research Letters*, *14*(8), 084034. https://doi.org/10.1088/1748-9326/AB304E

Edmonds, D. A., & Slingerland, R. L. (2007). Mechanics of river mouth bar formation: Implications for the morphodynamics of delta distributary networks. *Journal of Geophysical Research: Earth Surface*, *112*(2). https://doi.org/10.1029/2006JF000574

Edmonds, D. A., & Slingerland, R. L. (2008). Stability of delta distributary networks and their bifurcations. *Water Resources Research*, *44*(9), 9426. https://doi.org/10.1029/2008WR006992

Edmonds, D. A., & Slingerland, R. L. (2010). Significant effect of sediment cohesion on deltamorphology. *Nature Geoscience*, *3*(2), 105–109. https://doi.org/10.1038/ngeo730

Edmonds, D. A., Hoyal, D. C. J. D., Sheets, B. A., & Slingerland, R. L. (2009). Predicting delta avulsions: Implications for coastal wetland restoration. *Geology*, *37*(8), 759–762. https://doi.org/10.1130/G25743A.1

Edmonds, D. A., Paola, C., Hoyal, D. C. J. D., & Sheets, B. A. (2011). Quantitative metrics that describe river deltas and their channel networks. *Journal of Geophysical Research: Earth Surface*, *116*(4), 1–15. https://doi.org/10.1029/2010JF001955

Ericson, J. P., Vörösmarty, C. J., Dingman, S. L., Ward, L. G., & Meybeck, M. (2006). Effective sea-level rise and deltas: Causes of change and human dimension implications. *Global and Planetary Change*, *50*(1–2), 63–82. https://doi.org/10.1016/j.gloplacha.2005.07.004

Fagherazzi, S., Edmonds, D. A., Nardin, W., Leonardi, N., Canestrelli, A., Falcini, F., et al. (2015). Dynamics of river mouth deposits. *Reviews of Geophysics*, *53*(3), 642–672. https://doi.org/10.1002/2014RG000451

Ganti, V., Chadwick, A. J., Hassenruck-Gudipati, H. J., & Lamb, M. P. (2016). Avulsion cycles and their stratigraphic signature on an experimental backwater-controlled delta. *Journal of Geophysical Research: Earth Surface*, *121*(9), 1651–1675. https://doi.org/10.1002/2016JF003915

Ganti, V., Chadwick, A. J., Hassenruck-Gudipati, H. J., Fuller, B. M., & Lamb, M. P. (2016). Experimental river delta size set by multiple floods and backwater hydrodynamics. *Science Advances*, *2*(5), e1501768. https://doi.org/10.1126/sciadv.1501768

Ganti, V., Lamb, M. P., & Chadwick, A. J. (2019). Autogenic Erosional Surfaces in Fluvio-deltaic Stratigraphy from Floods, Avulsions, and Backwater Hydrodynamics. *Journal of Sedimentary Research*, *89*(8), 815–832. https://doi.org/10.2110/jsr.2019.40

Geleynse, N., Storms, J. E. A., Walstra, D. J. R., Jagers, H. R. A., Wang, Z. B., & Stive, M. J. F. (2011). Controls on river delta formation; insights from numerical modelling. *Earth and Planetary Science Letters*, *302*(1–2), 217–226. https://doi.org/10.1016/j.epsl.2010.12.013

Giosan, L., Syvitski, J., Constantinescu, S., & Day, J. (2014). Climate change: Protect the world's deltas. *Nature*, *516*(7529), 31–33. https://doi.org/10.1038/516031a

Hackney, C. R., Darby, S. E., Parsons, D. R., Leyland, J., Best, J. L., Aalto, R., et al. (2020). River bank instability from unsustainable sand mining in the lower Mekong River. *Nature Sustainability 2020 3:3*, *3*(3), 217–225. https://doi.org/10.1038/s41893-019-0455-3

Hartley, A. J., Weissmann, G. S., & Scuderi, L. (2017). Controls on the apex location of large deltas. *Journal of the Geological Society*, *174*(1), 10–13. https://doi.org/10.1144/jgs2015-154

Jerolmack, D. J. (2009). Conceptual framework for assessing the response of delta channel networks to Holocene sea level rise. *Quaternary Science Reviews*, *28*, 1786–1800. https://doi.org/10.1016/j.quascirev.2009.02.015

Jerolmack, D. J., & Mohrig, D. (2007). Conditions for branching in depositional rives. *Geology*, *35*(5), 463–466. https://doi.org/10.1130/G23308A.1

Jones, L. S., & Schumm, S. A. (2009). Causes of Avulsion: An Overview. *Fluvial Sedimentology VI*, 169–178. https://doi.org/10.1002/9781444304213.CH13

Jordan, C., Tiede, J., Lojek, O., Visscher, J., Apel, H., Nguyen, H. Q., et al. (2019). Sand mining in the Mekong Delta revisited - current scales of local sediment deficits. *Scientific Reports 2019 9:1*, *9*(1), 1–14. https://doi.org/10.1038/s41598-019-53804-z

Kleinhans, M. G., & Hardy, R. J. (2013, March 15). River bifurcations and avulsion. *Earth Surface Processes and Landforms*. John Wiley & Sons, Ltd. https://doi.org/10.1002/esp.3354

Kleinhans, M. G., Ferguson, R. I., Lane, S. N., & Hardy, R. J. (2013). Splitting rivers at their seams: bifurcations and avulsion. *Earth Surface Processes and Landforms*, *38*(1), 47–61. https://doi.org/10.1002/esp.3268

Lane, T. I., Nanson, R. A., Vakarelov, B. K., Ainsworth, R. B., & Dashtgard, S. E. (2017). Evolution and architectural styles of a forced-regressive Holocene delta and megafan, Mitchell River, Gulf of Carpentaria, Australia. *Geological Society Special Publication*, *444*(1), 305–334. https://doi.org/10.1144/SP444.9

Li, J., Ganti, V., Li, C., & Wei, H. (2022). Upstream migration of avulsion sites on lowland deltas with river-mouth retreat. *Earth and Planetary Science Letters*, *577*, 117270. https://doi.org/10.1016/J.EPSL.2021.117270

Loucks, D. P. (2019). Developed river deltas: are they sustainable? *Environmental Research Letters*, *14*(11), 113004. https://doi.org/10.1088/1748-9326/AB4165

McEwan, E., Stahl, T., Howell, A., Langridge, R., & Wilson, M. (2023). Coseismic river avulsion on surface rupturing faults: Assessing earthquake-induced flood hazard. *Science Advances*, *9*(18). https://doi.org/10.1126/SCIADV.ADD2932

Mohrig, D., Heller, P. L., Paola, C., & Lyons, W. J. (2000). Interpreting avulsion process from ancient alluvial sequences: Guadalope-Matarranya system (Northern Spain) and Wasatch formation (Western Colorado). *Bulletin of the Geological Society of America*, *112*(12), 1787–1803. https://doi.org/10.1130/0016-7606(2000)112<1787:IAPFAA>2.0.CO;2

Moodie, A. J., Nittrouer, J. A., Ma, H., Carlson, B. N., Chadwick, A. J., Lamb, M. P., & Parker, G. (2019). Modeling Deltaic Lobe-Building Cycles and Channel Avulsions for the Yellow River Delta, China. *Journal of Geophysical Research: Earth Surface*, *124*(11), 2438–2462. https://doi.org/10.1029/2019JF005220

Moran, K. E., Nittrouer, J. A., Perillo, M. M., Lorenzo-Trueba, J., & Anderson, J. B. (2017). Morphodynamic modeling of fluvial channel fill and avulsion time scales during early Holocene transgression, as substantiated by the incised valley stratigraphy of the Trinity River, Texas. *Journal of Geophysical Research: Earth Surface*, *122*(1), 215–234. https://doi.org/10.1002/2015JF003778

Morgan, J. A., Kumar, N., Horner-Devine, A. R., Ahrendt, S., Istanbullouglu, E., & Bandaragoda, C. (2020). The use of a morphological acceleration factor in the simulation of large-scale fluvial morphodynamics. *Geomorphology*, *356*, 107088. https://doi.org/10.1016/J.GEOMORPH.2020.107088

Muto, T. (2001). Shoreline Autoretreat Substantiated in Flume Experiments. *Journal of Sedimentary Research*, *71*(2), 246–254. https://doi.org/10.1306/091400710246

Muto, Tetsuji, & Steel, R. J. (1997). Principles of regression and transgression; the nature of the interplay between accommodation and sediment supply. *Journal of Sedimentary Research*, *67*(6), 994–1000. https://doi.org/10.1306/D42686A8-2B26-11D7-8648000102C1865D

Nienhuis, J. H., Ashton, A. D., Edmonds, D. A., Hoitink, A. J. F., Kettner, A. J., Rowland, J. C., & Törnqvist, T. E. (2020). Global-scale human impact on delta morphology has led to net land area gain. *Nature*, *577*(7791), 514–518. https://doi.org/10.1038/s41586-019-1905-9

Nienhuis, Jaap H., Törnqvist, T. E., & Esposito, C. R. (2018). Crevasse Splays Versus Avulsions: A Recipe for Land Building With Levee Breaches. *Geophysical Research Letters*, *45*(9), 4058–4067. https://doi.org/10.1029/2018GL077933

Nienhuis, Jaap H, Hoitink, A. J. F., & Törnqvist, T. E. (2018). Future Change to Tide-Influenced Deltas. *Geophysical Research Letters*, *45*, 3499–3507. https://doi.org/doi.org/10.1029/2018GL077638

Nijhuis, A. G., Edmonds, D. A., Caldwell, R. L., Cederberg, J. A., Slingerland, R. L., Best, J. L., et al. (2015). Fluvio-deltaic avulsions during relative sea-level fall. *Geology*, *43*(8), 719–722. https://doi.org/10.1130/G36788.1

Paola, C., Twilley, R. R., Edmonds, D. A., Kim, W., Mohrig, D., Parker, G., et al. (2011). Natural Processes in Delta Restoration: Application to the Mississippi Delta. *Annual Review of Marine Science*, *3*(1), 67–91. https://doi.org/10.1146/annurev-marine-120709-142856

Parker, G., Wilcock, P. R., Paola, C., Dietrich, W. E., & Pitlick, J. (2007). Physical basis for quasi-universal relations describing bankfull hydraulic geometry of single-thread gravel bed rivers. *Journal of Geophysical Research: Earth Surface*, *112*(4). https://doi.org/10.1029/2006JF000549

Pierik, H. J., Moree, J. I. M., van der Werf, K. M., Roelofs, L., Albernaz, M. B., Wilbers, A., et al. (2023). Vegetation and peat accumulation steer Holocene tidal–fluvial basin filling and overbank sedimentation along the Old Rhine River, The Netherlands. *Sedimentology*, *70*(1), 179–213. https://doi.org/10.1111/SED.13038

Prasojo, O. A., Hoey, T. B., Owen, A., & Williams, R. D. (2022). Slope break and avulsion locations scale consistently in global deltas. *Geophysical Research Letters*, e2021GL093656. https://doi.org/10.1029/2021GL093656

Prasojo, O. A., Hoey, T. B., Owen, A., & Williams, R. D. (2023a). Supporting Information Table S2: First order controls of avulsion in river deltas. https://doi.org/10.6084/m9.figshare.20654037.v2 [Dataset]

Prasojo, O. A., Hoey, T. B., Owen, A., & Williams, R. D. (2023b). Model runs: First order controls of avulsion in river deltas. https://doi.org/10.6084/m9.figshare.23912625.v1. [Dataset]

Ratliff, K. M., Hutton, E. W. H., & Murray, A. B. (2021). Modeling long-term delta dynamics reveals persistent geometric river avulsion locations. *Earth and Planetary Science Letters*, *559*, 116786. https://doi.org/10.1016/j.epsl.2021.116786

Reitz, M. D., Jerolmack, D. J., & Swenson, J. B. (2010). Flooding and flow path selection on alluvial fans and deltas. *Geophysical Research Letters*, *37*(6), n/a-n/a. https://doi.org/10.1029/2009GL041985

Rossi, V. M., Kim, W., López, J. L., Edmonds, D., Geleynse, N., Olariu, C., et al. (2016). Impact of tidal currents on delta-channel deepening, stratigraphic architecture, and sediment bypass beyond the shoreline. *Geology*, *44*(11), 927–930. https://doi.org/10.1130/G38334.1

Sanks, K. M., Zapp, S. M., Silvestre, J. R., Shaw, J. B., Dutt, R., & Straub, K. M. (2022). Marsh Sedimentation Controls Delta Top Morphology, Slope, and Mass Balance. *Geophysical Research Letters*, *49*(12), e2022GL098513. https://doi.org/10.1029/2022GL098513

Shields, M. R., Bianchi, T. S., Mohrig, D., Hutchings, J. A., Kenney, W. F., Kolker, A. S., & Curtis, J. H. (2017). Carbon storage in the Mississippi River delta enhanced by environmental engineering. *Nature Geoscience 2017 10:11*, *10*(11), 846–851. https://doi.org/10.1038/ngeo3044

Slingerland, R., & Smith, N. D. (2004). River Avulsions and Their Deposits. *Annual Review of Earth and Planetary Sciences*, *32*(1), 257–285. https://doi.org/10.1146/annurev.earth.32.101802.120201

Syvitski, J. P. M., & Saito, Y. (2007). Morphodynamics of deltas under the influence of humans. *Global and Planetary Change*, *57*(3–4), 261–282. https://doi.org/10.1016/j.gloplacha.2006.12.001

Syvitski, J. P. M., Kettner, A. J., Overeem, I., Hutton, E. W. H., Hannon, M. T., Brakenridge, G. R., et al. (2009). Sinking deltas due to human activities. *Nature Geoscience*, *2*(10), 681–686. https://doi.org/10.1038/ngeo629

Tessler, Z. D., Vorosmarty, C. J., Grossberg, M., Gladkova, I., Aizenman, H., Syvitski, J. P. M., & Foufoula-Georgiou, E. (2015). Profiling risk and sustainability in coastal deltas of the world. *Science*, *349*, 638–643. https://doi.org/10.1126/science.aab3574

Törnqvist, T. E. (1994). Middle and late Holocene avulsion history of the River Rhine (Rhine-Meuse delta, Netherlands). *Geology*, *22*(August), 711–714. Retrieved from http://pubs.geoscienceworld.org/gsa/geology/article-pdf/22/8/711/3515257/i0091-7613-22-8-711.pdf

Valenza, J. M., Edmonds, D. A., Hwang, T., & Roy, S. (2020). Downstream changes in river avulsion style are related to channel morphology. *Nature Communications*, *11*(2116). https://doi.org/10.1038/s41467-020-15859-9

Wallace, D. J., Storms, J. E. A., Wallinga, J., Dam, R. L. V. A. N., Blaauw, M., Derksen, M. S., et al. (2014). Shrinking and Sinking Deltas : Major role of Dams in delta subsidence and Effective Sea Level Rise. *Nature Geoscience*, *123*(May), 1973–1984. https://doi.org/10.1038/ngeo129

Williams, R. D., Measures, R., Hicks, D. M., & Brasington, J. (2016). Assessment of a numerical model to reproduce event-scale erosion and deposition distributions in a braided river. *Water Resources Research*, *52*(8), 6621–6642. https://doi.org/10.1002/2015WR018491

Wolinsky, M. A., Edmonds, D. A., Martin, J., & Paola, C. (2010). Delta allometry: Growth laws for river deltas. *Geophysical Research Letters*, *37*(21). https://doi.org/10.1029/2010GL044592

Wright, L. D. (1977). Sediment transport and deposition at river mouths: A synthesis. *Bulletin of the Geological Society of America*, *88*(6), 857–868. https://doi.org/10.1130/0016-7606(1977)88<857:STADAR>2.0.CO;2

Figure 1.

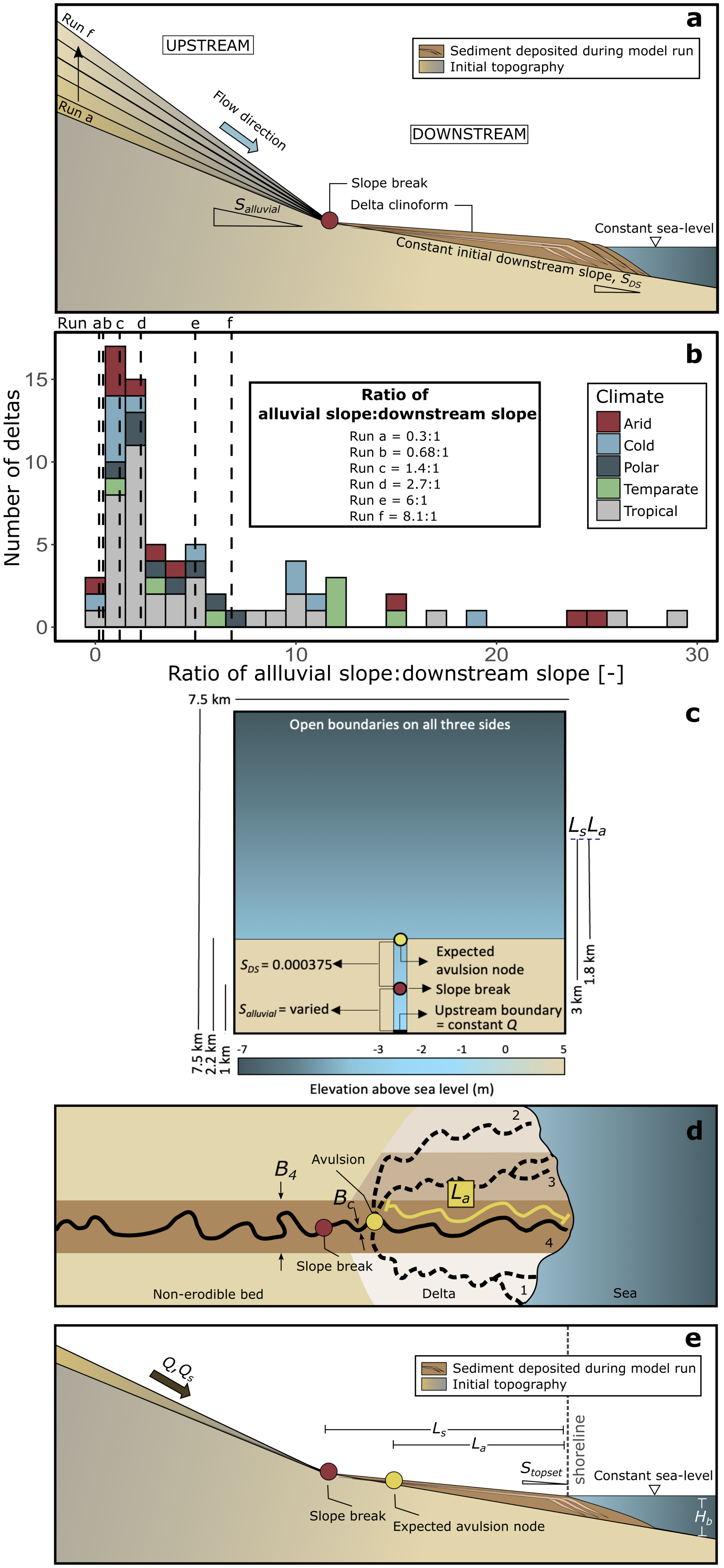

a
Run f
Run a
UPSTREAM
Flow direction
DOWNSTREAM
Sediment deposited during model run
Initial topography
Slope break
Delta clinoform
$S_{alluvial}$
Constant sea-level
Constant initial downstream slope, S_{DS}
b
Run a b c d e f
Ratio of alluvial slope:downstream slope
Run a = 0.3:1
Run b = 0.68:1
Run c = 1.4:1
Run d = 2.7:1
Run e = 6:1
Run f = 8.1:1
Climate
Arid
Cold
Polar
Temparate
Tropical
Number of deltas
Ratio of allluvial slope:downstream slope [-]
c
7.5 km
Open boundaries on all three sides
L_s L_a
S_{DS} = 0.000375
Expected avulsion node
Slope break
$S_{alluvial}$ = varied
Upstream boundary = constant Q
1.8 km
3 km
7.5 km
2.2 km
1 km
-7 -3 -2 -1 0 5
Elevation above sea level (m)
d
B_4
Avulsion
B_c
L_a
Slope break
Non-erodible bed
Delta
Sea
1 2 3 4
e
Q, Q_s
Sediment deposited during model run
Initial topography
L_s
L_a
shoreline
S_{topset}
Constant sea-level
H_b
Slope break
Expected avulsion node

Figure 2.

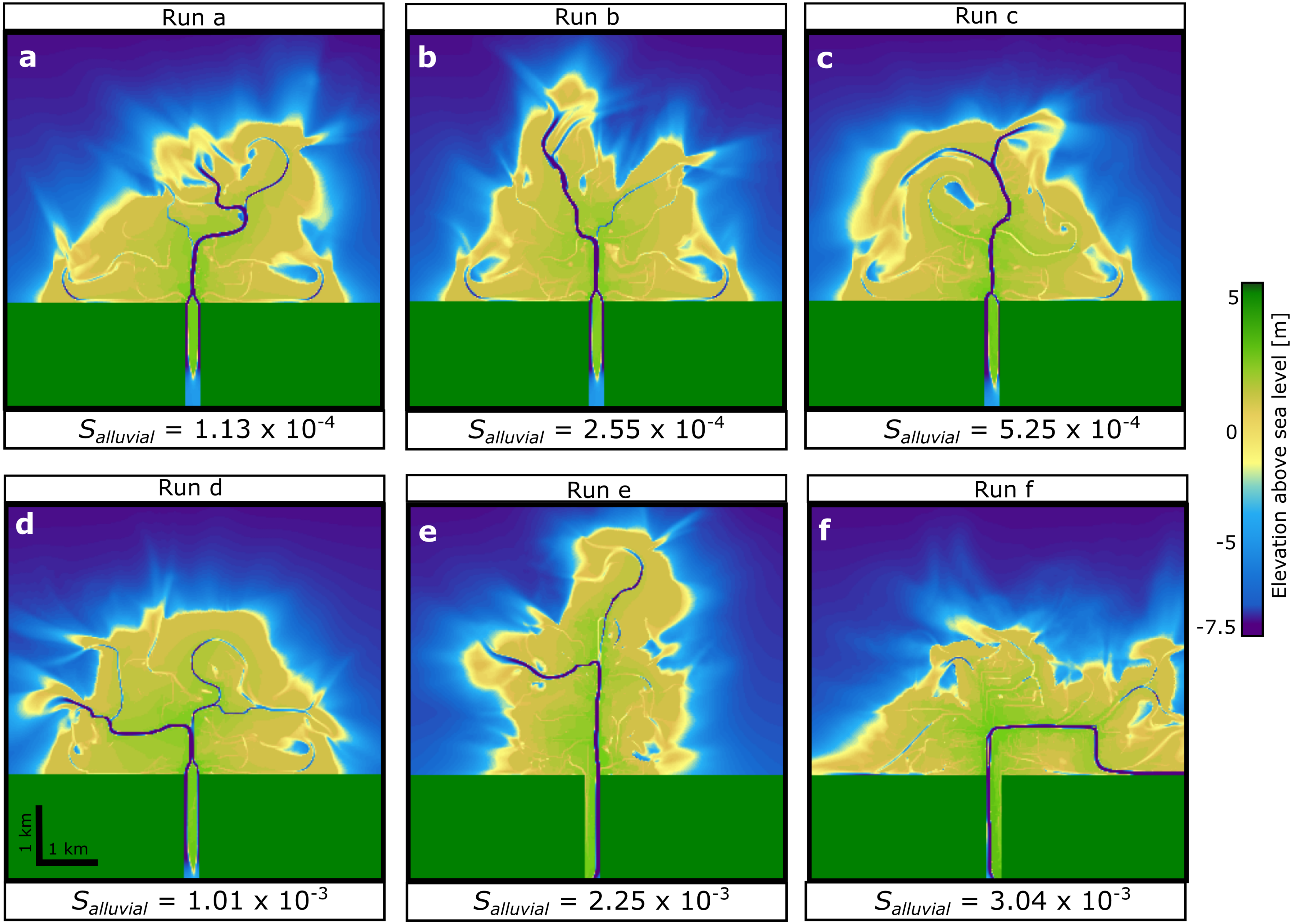

Run a
a
$S_{alluvial}$ = 1.13 x 10^{-4}
Run b
b
$S_{alluvial}$ = 2.55 x 10^{-4}
Run c
c
$S_{alluvial}$ = 5.25 x 10^{-4}
Run d
d
1 km
1 km
$S_{alluvial}$ = 1.01 x 10^{-3}
Run e
e
$S_{alluvial}$ = 2.25 x 10^{-3}
Run f
f
$S_{alluvial}$ = 3.04 x 10^{-3}
Elevation above sea level [m]
5
0
-5
-7.5

Figure 3.

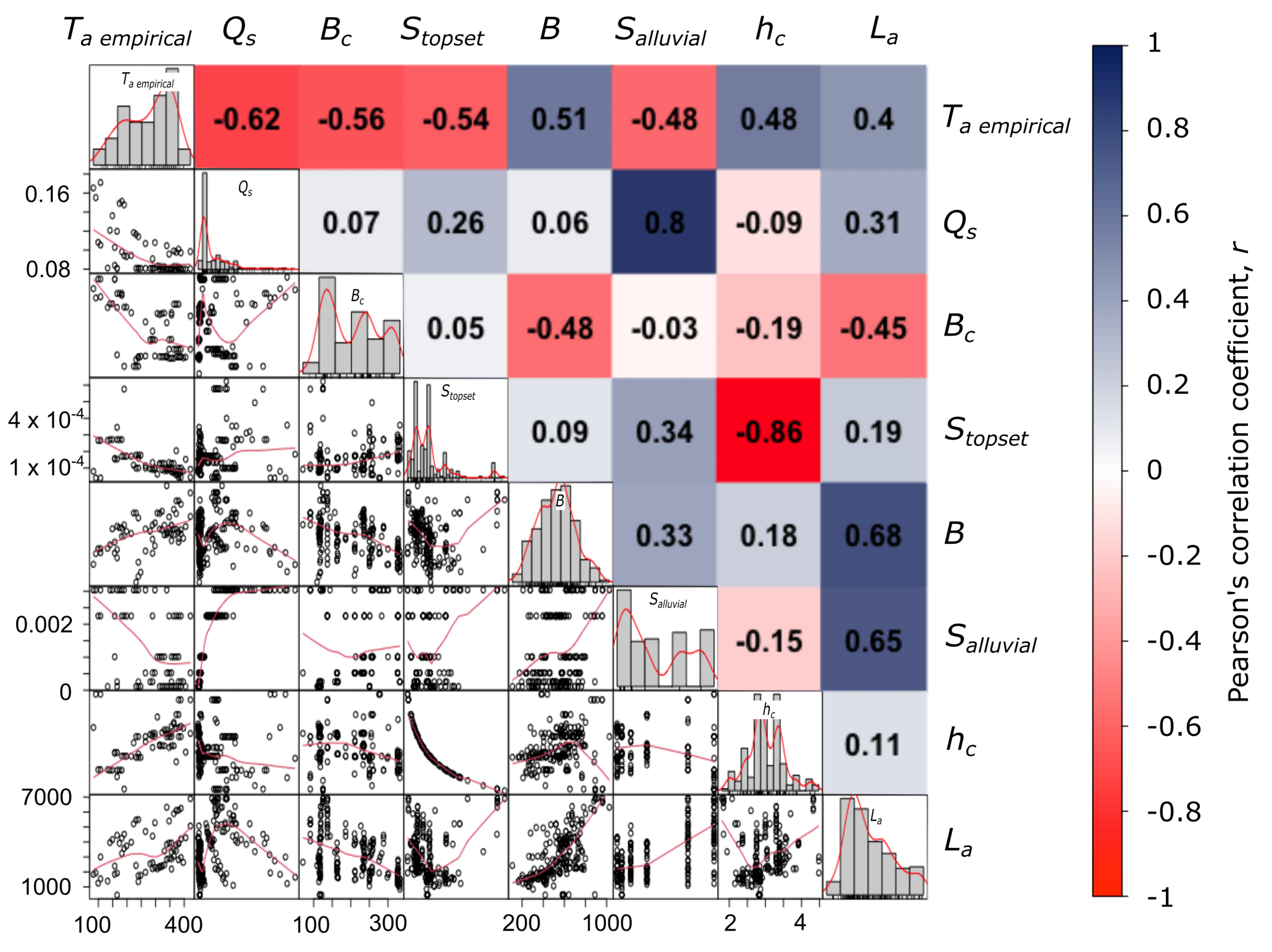

$T_{a\ empirical}$
Q_s
B_c
S_{topset}
B
$S_{alluvial}$
h_c
L_a
-0.62
-0.56
-0.54
0.51
-0.48
0.48
0.4
0.07
0.26
0.06
0.8
-0.09
0.31
0.05
-0.48
-0.03
-0.19
-0.45
0.09
0.34
-0.86
0.19
0.33
0.18
0.68
-0.15
0.65
0.11
0.16
0.08
4 x 10^{-4}
1 x 10^{-4}
0.002
0
7000
1000
100
400
100
300
200
1000
2
4
1
0.8
0.6
0.4
0.2
0
-0.2
-0.4
-0.6
-0.8
-1
Pearson's correlation coefficient, r

Figure 4.

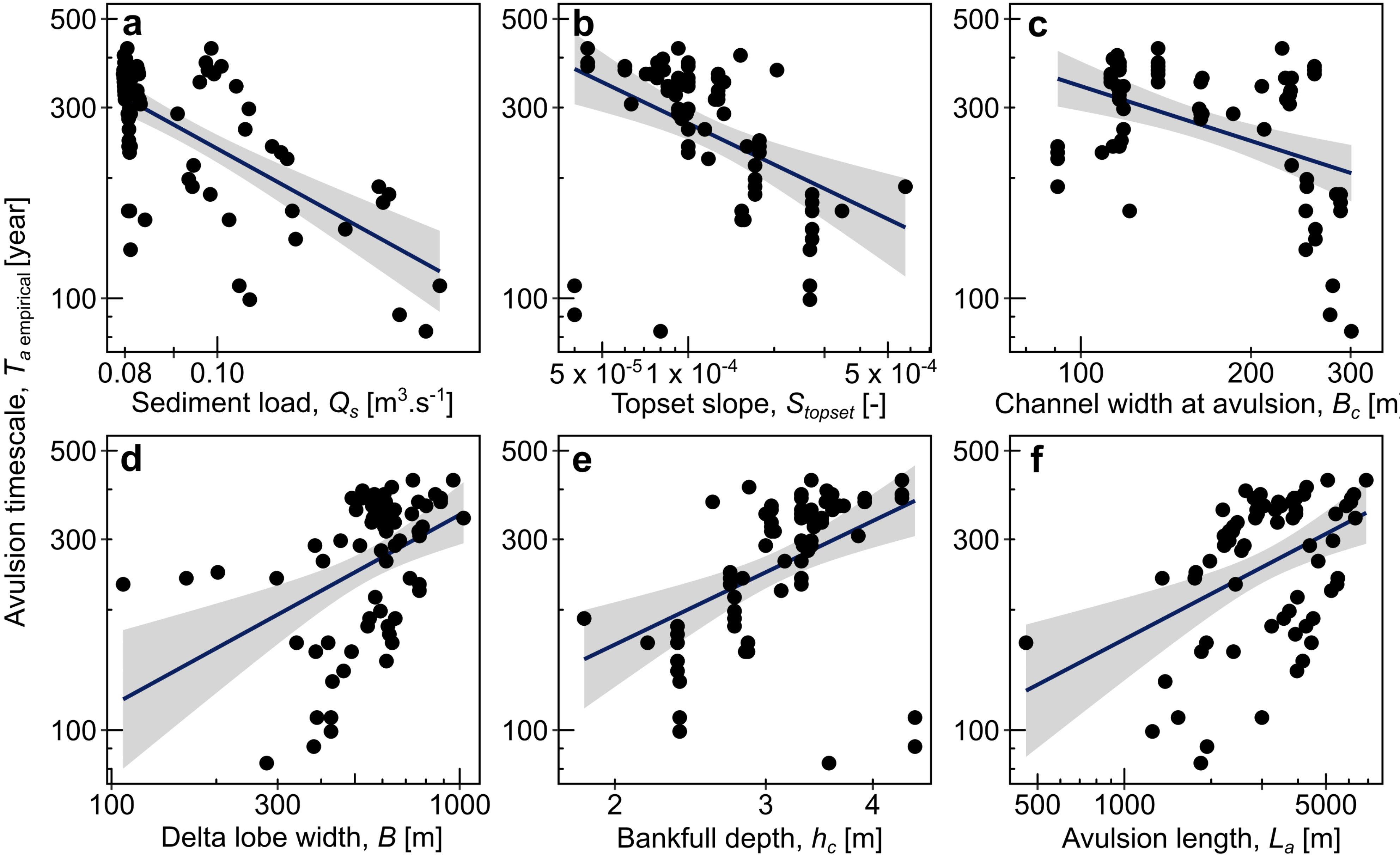

$T_{a\ \mathrm{empirical}} = 11.45Q_s^{-1.32}$, $R^2 = 0.38$, $p = 6.76 \times 10^{-10}$, $SE_{\mathrm{residual}} = 0.32$

$T_{a\ \mathrm{empirical}} = 11.7S_{topset}^{-0.34}$, $R^2 = 0.23$, $p = 1.4 \times 10^{-4}$, $SE_{\mathrm{residual}} = 0.38$

$T_{a\ \mathrm{empirical}} = 4572.6B_c^{-0.56}$, $R^2 = 0.21$, $p = 1.76 \times 10^{-6}$, $SE_{\mathrm{residual}} = 0.32$

$T_{a\ \mathrm{empirical}} = 12.77B^{0.48}$, $R^2 = 0.24$, $p = 1.74 \times 10^{-4}$, $SE_{\mathrm{residual}} = 0.38$

$T_{a\ \mathrm{empirical}} = 80.34h_c^{1.03}$, $R^2 = 0.23$, $p = 1.38 \times 10^{-4}$, $SE_{\mathrm{residual}} = 0.38$

$T_{a\ \mathrm{empirical}} = 12.45L_a^{0.38}$, $R^2 = 0.18$, $p = 2.18 \times 10^{-4}$, $SE_{\mathrm{residual}} = 0.38$

Figure 5.

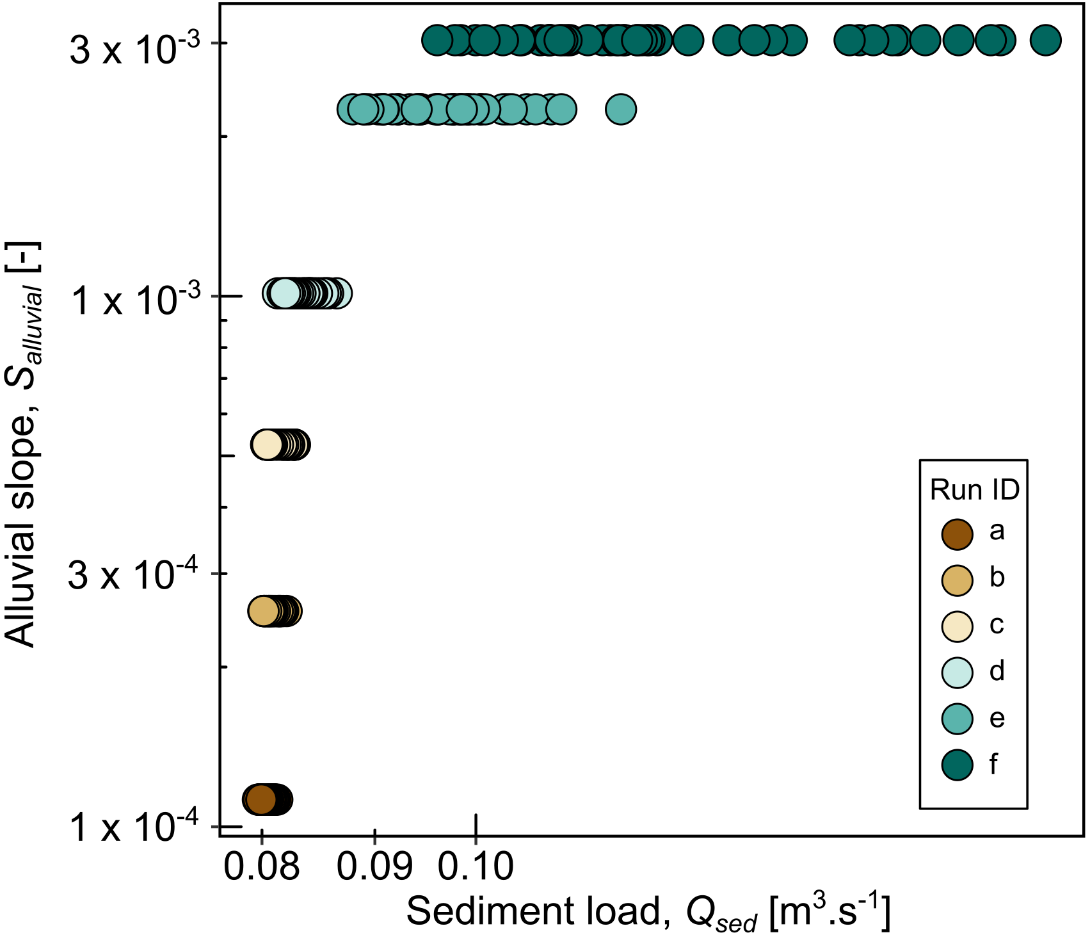

3 x 10-3
1 x 10-3
3 x 10-4
1 x 10-4
Alluvial slope, $S_{alluvial}$ [-]
0.08
0.09
0.10
Sediment load, Q_{sed} [$m^3.s^{-1}$]
Run ID
a
b
c
d
e
f

Figure 6.

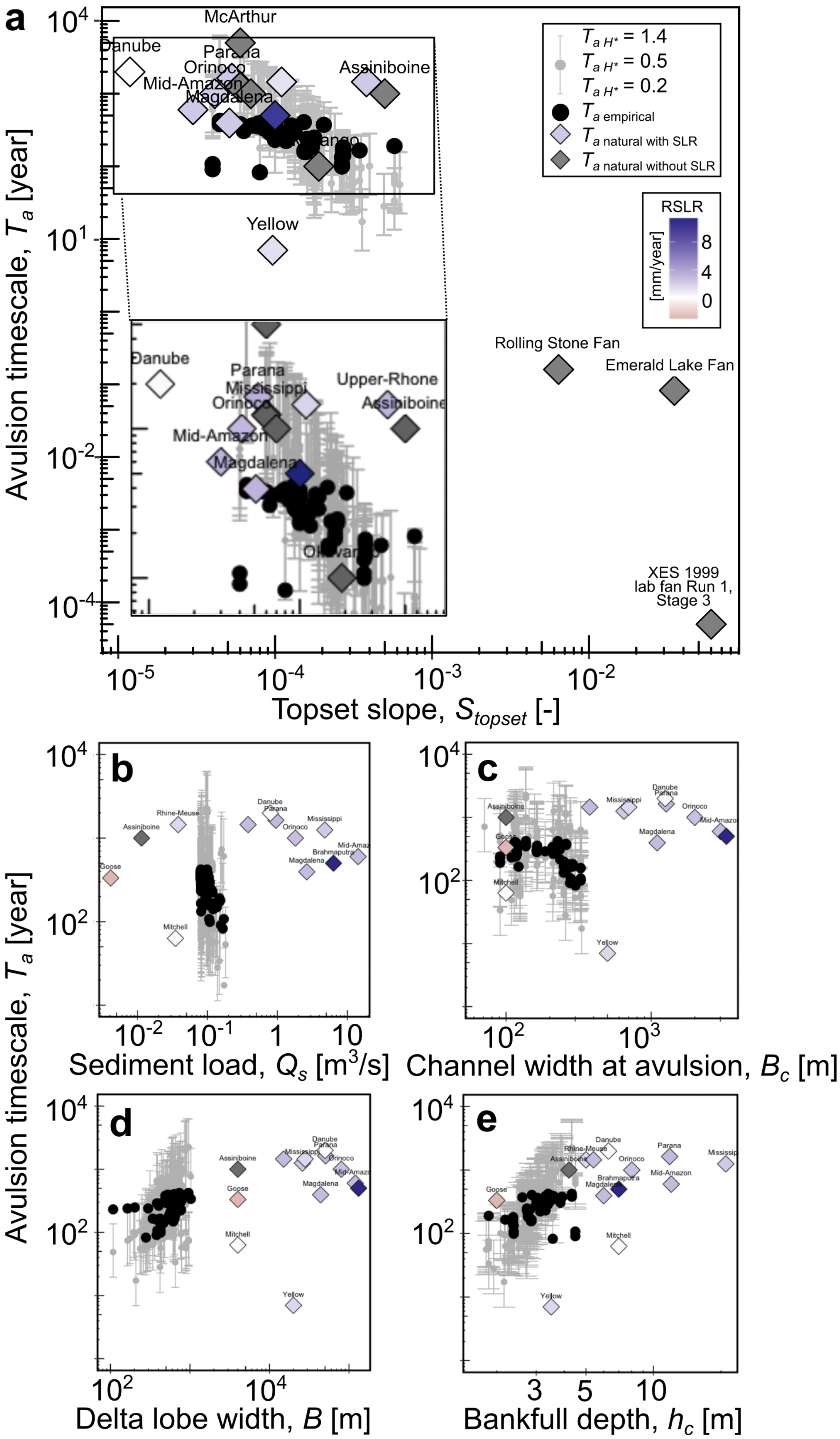
a
b
c
d
e
McArthur
Danube
Parana
Orinoco
Mid-Amazon
Magdalena
Assiniboine
Okavango
Yellow
Mississippi
Upper-Rhone
Rolling Stone Fan
Emerald Lake Fan
XES 1999
lab fan Run 1,
Stage 3
$T_{a\,H^*}$ = 1.4
$T_{a\,H^*}$ = 0.5
$T_{a\,H^*}$ = 0.2
T_a empirical
T_a natural with SLR
T_a natural without SLR
RSLR
[mm/year]
Avulsion timescale, T_a [year]
Topset slope, S_{topset} [-]
Rhine-Meuse
Goose
Mitchell
Brahmaputra
Sediment load, Q_s [m^3/s]
Channel width at avulsion, B_c [m]
Delta lobe width, B [m]
Bankfull depth, h_c [m]